August 2019

Construction of Bismuth Oxyhallide-based Heterojunction-structured Composite and Its Environmental Application for Water Treatment

Li Wang
University of Wisconsin-Milwaukee

CONSTRUCTION OF BISMUTH OXYHALIDE-BASED HETEROJUNCTION-STRUCTURED COMPOSITE AND ITS ENVIRONMENTAL APPLICATION FOR WATER TREATMENT

by

Li Wang

A Thesis Submitted in

Partial Fulfillment of the

Requirements for the Degree of

Master of Science

in Engineering

at

The University of Wisconsin-Milwaukee

August 2019

ABSTRACT

CONSTRUCTION OF BISMUTH OXYHALIDE-BASED HETEROJUNCTION-STRUCTURED COMPOSITE AND ITS ENVIRONMENTAL APPLICATION FOR WATER TREATMENT

by

Li Wang

The University of Wisconsin-Milwaukee, 2019
Under the Supervision of Professor Yin Wang

With the rapid development of the global economy, environmental protection and sustainable development have become the main trends of current society. In particular, water pollution and energy shortage are outstanding issues that need to be solved in a clean and sustainable way. Recently, semiconductor-based photocatalytic technology, an environmentally friendly technique, has attracted enormous attention and become an emerging research hotspot in the application of water/wastewater treatment and generation of renewable energy as it can convert infinite solar energy into chemical energy. Conventional semiconductor materials usually have a relatively large band gap that only responds to the ultraviolet light, which largely limits their practical applications. Therefore, design of novel efficient photocatalytic materials that can be excited by visible light or solar light is a promising research direction.

Bismuth oxyhalides have been drawing increasing interest as promising photocatalysts for their suitable band gaps, low cost, nontoxicity and chemical stability. Besides, formation of heterojunction structure by coupling two or more semiconductors is usually considered as an effective approach to further improve the photocatalytic activities of catalysts. Hence, in this study, $BiOBr/Bi_{12}O_{17}Cl_2$ heterojunction-structured materials were synthesized by a facile *in situ* chemical deposition-precipitation method and a series of characterization methods were employed to

analyze the as-prepared samples. The photocatalytic properties were investigated by degrading several typical model organic contaminants under the irradiation of simulated solar light or visible light. The BiOBr/$Bi_{12}O_{17}Cl_2$ composite exhibited superior photocatalytic performance over pure BiOBr and $Bi_{12}O_{17}Cl_2$. Additionally, the mass ratio between BiOBr and $Bi_{12}O_{17}Cl_2$ was optimized to get the heterojunction composite with highest photocatalytic activity. What's more, the plausible reason for such enhancement of photocatalytic reaction and a possible photocatalytic mechanism interpreted through the quenching effect of different scavengers were discussed. The present work could provide a facile strategy to synthesize novel highly efficient and stable bismuth-based photocatalysts at room temperature for environmental applications.

TABLE OF CONTENTS

LIST OF FIGURES

LIST OF TABLES

LIST OF ABBREVIATIONS

2D	Two dimensional
3D	Three dimensional
4-CP	4-chlorophenol
AO	Ammonium oxalate
AOPs	Advanced oxidation processes
BET	Brunauer–Emmett–Teller
BQ	p-Benzoquinone
BiOX	Bismuth oxyhalide
CB	Conduction band
DFT	Density functional theory
DRS	Diffuse reflectance spectra
EDS	Energy dispersive X-ray spectroscopy
EG	Ethylene glycol
E_g	Band gap energy
EIS	Electrochemical impedance spectroscopy
FT-IR	Fourier transform infrared
HPLC	High performance liquid chromatography
IPA	Isopropanol (2-Propanol)
MO	Methyl orange
NIR	Near-infrared
PL	Photoluminescence

rGO	Reduced graphene oxide
SEM	Scanning electron microscopy
TC	Tetracycline
TEM	Transmission electron microscopy
UV	Ultraviolet
UV-vis	Ultraviolet visible
VB	Valance band
XPS	X-ray photoelectron spectroscopy
XRD	X-ray diffraction

ACKNOWLEDGEMENTS

First of all, I would like to express my sincere gratitude to my advisor, Professor Yin Wang, for his support and advice for my study and research at UW-Milwaukee. I have learned a lot of things from Dr. Wang, including his passion and rigorous attitude for research, which inspire me to pursue a higher standard for research and life. He also provided us a relatively relaxed and free academic atmosphere, where we can deploy our own ideas and feel the fun of doing experiments. It's a truly privilege being his student and I would like to extend my thanks for everything he's done for me, which made me have a period of unforgettable time.

Then, I would like to thank all members in Dr. Wang's group for their help during my study and research. In particular, I want to thank Xiaopeng Min for his assistance of taking TEM image and the training of HPLC. Also, I want to thank Xiaoyu Sui in Dr. Chen's lab for his assistance of conducting SEM analysis. Meanwhile, I want to acknowledge Dr. Steven Hardcastle from Advanced Analysis Facility of CEAS at UWM for his technical support for parts of characterizations of materials. Likewise, I want to thank everyone who helped me during my study at UWM.

Furthermore, I am grateful for my thesis committee members for spending their valuable time guiding and advising in my thesis defense and dissertation.

Finally, I want to give my biggest thanks to my parents, wife and lovely daughter for their endless patience and support and it's your selfless love make me go forward and be a better man whenever I face difficulties. Love you all!

Chapter 1 Introduction and Literature Review

With the development of society and economy, we are now increasingly facing serious issues of energy shortage and environmental pollution. It is thus imperative to resolve the pollution problems of surface water and groundwater as the scarcity of freshwater resources and importance of clean water for a variety of crucial industries. Also, the presence of large amounts of contaminants in the aquatic environment would result in ecological and health hazards. These problems cause a growing demand for effective environmental remediation and energy conversion techniques. Conventional water and wastewater treatment methods consist of physical, chemical and biological processes. However, physical process usually merely covers phase transfer and pollutants themselves cannot be degraded even if it sometimes has pretty high reduction efficiency, such as adsorption or membrane separation of contaminants. For chemical process, it generally needs the application of a lot of chemical oxidants, which is not cost-effective or producing harmful by-products even if they can mineralize the pollutants with relatively high efficiency. For biological process, it normally takes a relatively long period of time to effectively degrade organic compounds in water as it imitates the activity of microorganisms, and there are also a large amount of nonbiodegradable compounds present in water/wastewater. [1] In addition, the search for clean and sustainable energy resources is important as well to address the energy demand and climate change. Hence, more and more efforts are being made to develop new approaches with lower cost and shorter time to deal with water and wastewater and to investigate alternative energies to tackle energy shortages.

Among various renewable energy resources, solar energy represents the ultimate sustainable source. To date, it remains a significant challenge to efficiently harvest and convert

solar energy. Since the Japanese scientists Honda and Fujishima[2] made a breakthrough in photocatalysis research in 1972 showing that water could be split into oxygen and hydrogen after light irradiation on a titanium dioxide (TiO_2) semiconductor electrode, the semiconductor-based photocatalytic technology, a kind of environmental-friendly advanced oxidation processes (AOPs), has been shown to be quite promising for renewable energy generation (such as water decomposition and reduction of carbon dioxide) and environmental remediation through using the inexhaustible. From then on, more and more research efforts are focusing on photocatalysis as a means of solar energy conversion given that solar energy is recognized as the ultimate renewable source, and the key requirement to achieve highly efficient photocatalytic process is the rational design of photocatalytic materials.

1.1 Homogeneous photocatalysis

Photocatalysis is the acceleration of a chemical reaction by the irradiation of light on a catalyst. Generally, photocatalysis can be divided into two categories, homogeneous photocatalysis and heterogeneous photocatalysis. In homogeneous photocatalysis, the photocatalysts and the reactants exist in the same phase, and the most studied homogeneous photocatalysis processes include ozonation, UV(ultraviolet)/hydrogen peroxide (H_2O_2), as well as the Fenton and photo-Fenton processes (Fe^+ and Fe^+/H_2O_2). [3] Commonly, these aqueous phase oxidation processes are based primarily on the production of hydroxyl radical (HO•) to destruct target pollutants. The generation of free radicals is accelerated by combining specific oxidizing agents such as H_2O_2 and ferrous iron. Specifically, the photo-Fenton process that consists of the combination of the classical Fenton reaction with the photo-assisted regeneration of Fe^{2+} from Fe^{3+} (Equations 1 – 2) is one of the most researched homogeneous photocatalysis process. [4] This process can work by irradiation of the solution up to a light wavelength of 600 nm[3]. However,

the drawbacks of this process include that the low pH (2.8-3.5)[4] values are required to avoid any precipitation of inactive iron oxyhydroxides, and the large amounts of dissolved iron needed to be removed after treatment.

$$Fe^{3+} + hv + H_2O \rightarrow Fe^{2+} + HO\cdot + H^+ \quad (1)$$

$$Fe^{2+} + H_2O_2 \rightarrow Fe^{3+} + HO\cdot + OH^- \quad (2)$$

1.2 Heterogeneous photocatalysis

For heterogeneous photocatalysis, the catalyst is present in a different phase from the reactants, and thus it can be easily recycled than the homogeneous one. Generally, heterogeneous photocatalysis refers to photoreactions with the use of semiconductor-based photocatalyst materials, where reactions occur on the surface of the photocatalyst. Compared to homogeneous photocatalysis and other water treatment options, heterogeneous photocatalysis has emerged as a fascinating technique because of its economic, nontoxic, safe and renewable features, and it has attracted considerable attention in the development of renewable energies,[5] water and wastewater treatment[6] and photosynthesis of value-added compounds[7] etc. The mechanism of heterogeneous photocatalysis is primarily described by the semiconductors' capability to generate charge carriers under light irradiation followed by the generation of free radicals such as OH• which leads to further reactions. When it comes to the treatment of water contaminated by organic compounds, the advantages of semiconductor-based heterogeneous photocatalysis are that the reaction could be carried out under mild condition (e.g., ambient temperature), the process may completely decompose organic pollutants into carbon dioxide and other inorganic species, and the catalyst can be reused etc.[8]

1.3 Fundamental principles of semiconductor-based photocatalysis

The principle of semiconductor photocatalysis is based on solid band energy theory. According to the band theory, the energy band of the semiconductor is discontinuous, which usually consists of a lower energy valance band (VB) filled with electrons and a higher energy unoccupied conduction band (CB), in which the electrons can move freely. The energy difference between valance band and conduction band is called bandgap, also known as the forbidden band (E_g). On the other hand, the size of band gap determines the range of light wavelength which the semiconductor can effectively absorb, and the positions of conduction band and valence band determine the redox ability of corresponding semiconductors in the photocatalytic reactions. Figure 1.1 shows the bandgaps and band positions of some typical semiconductors that have been widely studied in the photocatalysis field.

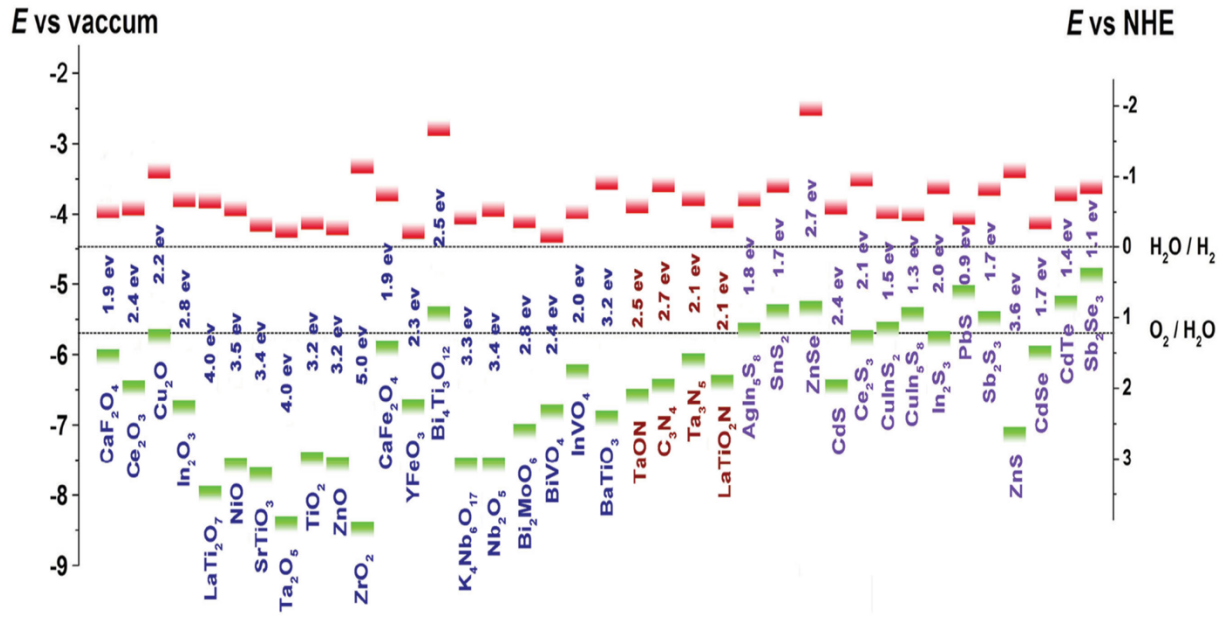

Figure 1.1 Bandgaps and band-edge positions with respect to the vacuum level and NHE for selected semiconductors. The horizontal red lines represent the conduction-band edges. The horizontal green lines represent the valence-band edges.[9]

A given semiconductor photocatalyst can absorb and be excited by the incoming light (photon energy equals to or greater than its corresponding bandgap energy), and then convert the photon energy into chemical energy. The typical photocatalytic oxidation and reduction processes following reaction with electron acceptors (A) and donors (D) on a semiconductor are presented in Figure 1.2. Upon an appropriate light irradiation, the absorption of photons excites the negatively charged electrons from the valance band of the semiconductor which creates electron vacancies in the valance band that can be thought of as positively charged holes to the conduction band to form photo-induced electron/hole (e^-/h^+) pairs, transforming the semiconductor catalyst into the photoexcited state. Secondly, the photo-generated electron-hole pairs are separated and subsequently migrated to their active sites on the surface of the semiconductor photocatalyst, and they can participate in various oxidation and reduction reactions, thereby initiating redox chemical reactions with the adsorbed species. The photogenerated electrons and holes act as the reductant and oxidant to react with the electron acceptors (A) and electron donors (D) adsorbed on the semiconductor surface, respectively.[10] Besides, the recombination of photo-induced charge carriers on the surface or in the bulk of the semiconductor can also occur, dissipating the energy in the form of heat or emitted light. To achieve higher photocatalytic performance of a specific semiconductor photocatalyst, the photo-induced electron-hole pairs should be efficiently separated, suppressing the recombination of electrons and holes.

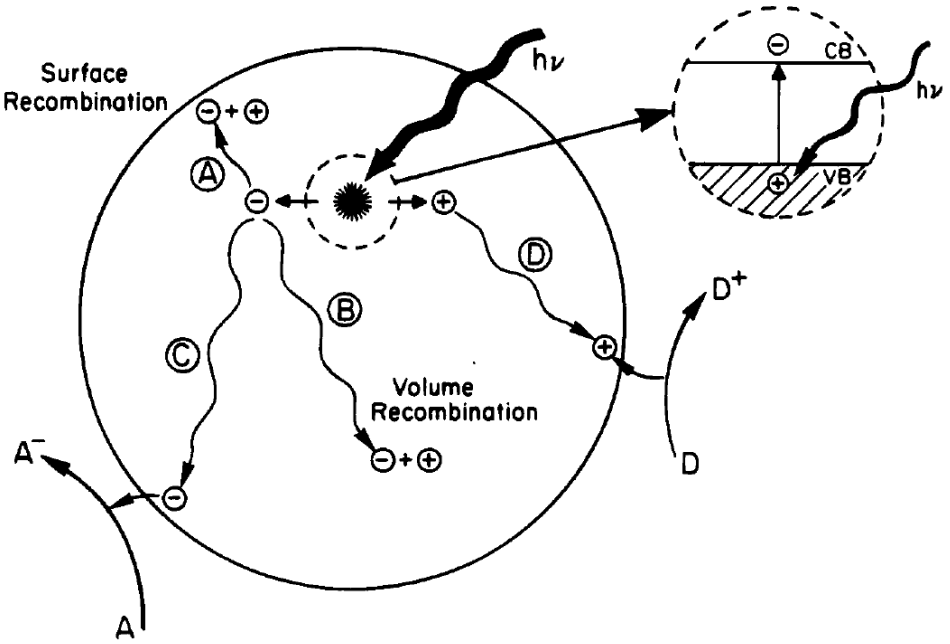

Figure 1.2 Schematic photoexcitation in a semiconductor photocatalyst followed by deexcitation paths.[11]

So far, a number of semiconductor materials have been investigated for numerous applications in the photocatalysis field, such as TiO_2[12], WO_3[13], ZnO[14], CdS[15] and so on. Among them, the TiO_2 semiconductor is widely considered as one of the excellent photocatalysts for oxidative decomposition of various organic compounds and water splitting due to its versatile, economical, stable, abundant, non-toxic and environmental-friendly properties. However, TiO_2, with a large bandgap of around 3.2 eV, can only absorbs and be excited by ultraviolet light, which accounts for about 4% of the incoming solar light spectrum on earth.[16] In contrast, visible light and near-infrared (NIR) light contain > 90% of the solar light energy. In order to extend the optical response wavelength range of TiO_2, a variety of ways have been applied to enhance its light absorption and photocatalytic performance in the visible light region or full-spectrum light, including doping, deposition of cocatalyst, coupling with other conductive materials or semiconductors of different energy levels, etc.

For instance, doping TiO_2 with nonmetals has received specific attention nowadays. Yang and co-workers[16] synthesized N-doped anatase TiO_2 samples through a solvothermal method, and characterization results showed that the nitrogen dopant had a significant effect on the crystallite size and optical absorption of TiO_2, improving the absorption in the visible light region and exhibiting better photocatalytic degradation activity for model dyes under visible light irradiation. Zhu et al.[17] prepared a visible-light active S-doped TiO_2 by a facile solvothermal approach, which displayed excellent photocatalytic performance toward the degradation of organic pollutants under visible and indoor sunlight illumination. Various kinds of cocatalysts have been applied on TiO_2 to improve the photocatalytic activity by reducing recombination rate of photo-induced charge carriers, of which loading metal cocatalysts are pretty common. For example, Chaker et al.[18] fabricated silver (Ag) doped mesoporous TiO_2 catalysts by impregnation-reduction method, and the photocatalytic activity for degradation of methyl orange (MO) under UV and simulated solar light was enhanced compared to the undoped catalyst.

Modifying TiO_2 with graphene substance, which is conductive and beneficial to separation of photo-generated electron/hole pairs, has been regarded as an effective way to enhance its photocatalytic performance. Pu et al.[19] demonstrated a facile and environmental-friendly strategy for *in situ* preparation of TiO_2@rGO (i.e., reduced graphene oxide), and the obtained TiO_2@rGO had a relatively high photocatalytic performance in the degradation reactions compared to commercial TiO_2. Forming heterojunction by combining two or more semiconductors is another promising approach to reduce the recombination rate to achieve a higher photocatalytic activity. For example, Li et al.[20] synthesized g-C_3N_4@TiO_2 nanostructures with hollow sphere morphology by the annealing method, and the obtained samples showed good photocatalytic property for hydrogen generation under visible light irradiation. Although the modification of TiO_2

through the abovementioned methods can extend its response under visible light irradiation to some degree, its photocatalytic efficiency over a broad range of light spectrum other than ultraviolet light is still relatively low, making it difficult for practical applications under solar light. In addition to modification of commonly studied semiconductor materials, such as TiO_2, another research direction in photocatalysis is to develop novel photocatalytic materials which can be driven by visible light or simulated sunlight.

1.4 Bismuth-based photocatalytic materials

Recently, bismuth-based nanomaterials have drawn considerable interest as promising candidates of photocatalysts for photocatalytic applications due to their narrow bandgaps, nontoxicity and low costs. It is noteworthy that the valance band mainly comprises of the 6s orbital of Bi and the 2p orbital of oxygen in the electronic structure of bismuth-based materials, and this crucial feature results in bismuth-based materials having bandgaps less than 3.0 eV. These well diffused Bi 6s and O 2p orbitals result in good dispersion of charge carriers and therefore decreases the bandgap of the materials.[21] Several bismuth-based semiconductor materials have been widely explored in the photocatalysis field, including $BiVO_4$, Bi_2MO_6 (M=Mo, W), BiOX (X=Cl, Br, I) and so on.

1.4.1 Bismuth vanadate ($BiVO_4$)

$BiVO_4$ has attracted significant attention owing to its outstanding features, such as plentiful abundance, low bandgap, non-toxicity, resistance to photo-corrosion and good photocatalytic performance in organic pollutant degradation under visible-light or sunlight irradiation. There are three crystal structures of $BiVO_4$, namely monoclinic, orthorhombic and tetragonal crystal systems, among which the monoclinic one with a bandgap of around 2.4 eV exhibits better photocatalytic activity compared to the other two kinds.[22] Phase transition from tetragonal to monoclinic occurs

irreversibly at about 400-500 ºC. The basic structural unit is constructed by VO_4 tetrahedron and BiO_8 dodecahedron, as show in Figure 1.3. Moreover, the Bi atoms and V atoms arrange alternately along the crystallographic axis, making monoclinic $BiVO_4$ exhibit the characteristics of layered structure.[23] Nevertheless, one limitation of the photocatalytic efficiency in $BiVO_4$ is the fast recombination rate of photo-induced charge carriers because of its narrow bandgap energy. To further enhance the photocatalytic activity, a series of strategies have been adopted to improve the separation of photogenerated electron-hole pairs, such as morphology control, selectively depositing cocatalyst on reactive facets and coupling other semiconductors to construct heterostructures.

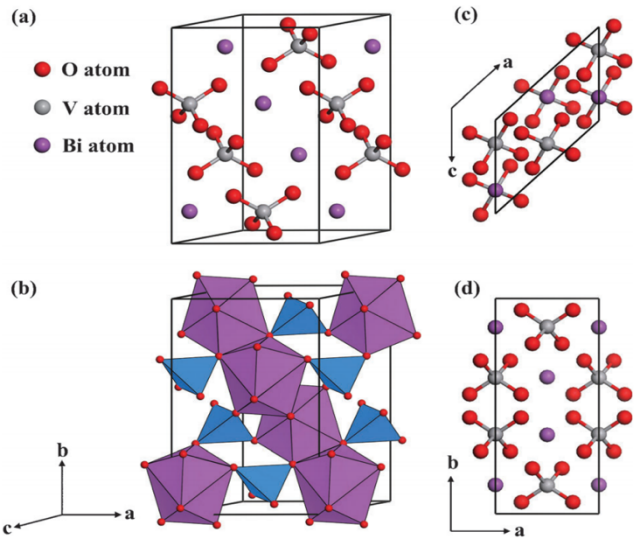

Figure 1.3 (a) The crystal structure of monoclinic $BiVO_4$ and (b) the corresponding polyhedron structure (blue: VO_4 tetrahedron, purple: BiO_8 dodecahedron); (c) top view and (d) side view of the structure.[23]

For instance, Hu et al.[24] fabricated a novel oxygen-rich monoclinic $BiVO_4$ nanotubes with largely exposed active {010} facets that displayed impressive photocatalytic performance. Dong et al.[25] synthesized ultrathin 2D $BiVO_4$ nanosheets with monoclinic crystal structure and uniformly distributed oxygen vacancies through a convenient colloidal two-phase method, and the as-prepared sample largely exposed {010} planes. As a result, this ultrathin $BiVO_4$ nanosheets

exhibited a superior photocatalytic activity for water oxidation under visible light irradiation. Li and co-workers selectively deposited the reduction and oxidation cocatalysts on the {010} and {110} facets respectively, leading to much higher photocatalytic water oxidation reactions.[26] A new pattern of Z-scheme heterojunction photocatalyst composed of $BiVO_4$ nanowires and CdS nanoparticles was synthesized,[27] which demonstrated broader light absorption region and increased photocatalytic hydrogen (H_2) generation.

1.4.2 Bi_2MO_6 (M=Mo, W) compounds

Bi_2MO_6 (M=Mo, W) materials are the simplest members of Aurivillius family, and they possess a layered structure which is composed of MO_6 octahedral layers and Bi-O-Bi layers, which can facilitate the transfer of the excited charge carriers and have attracted special attention. Also, the MO_6 (M=Mo, W) octahedrons are connected to each other by corner-sharing oxygen (O) atom and are sandwiched between the $[Bi_2O_2]^{2+}$ layers,[28] as shown in Figure 1.4. As Bi-based ternary metal oxide photocatalysts, they usually display a certain level of photocatalytic activities under visible light irradiation because of the unique physical and chemical properties, such as chemical inertness, photo stability and environmental friendliness. Different from $BiVO_4$, Bi_2MO_6 materials have two crystalline phases: monoclinic and orthorhombic structures. Moreover, the current studied Bi_2MO_6 photocatalysts are commonly orthorhombic phase.

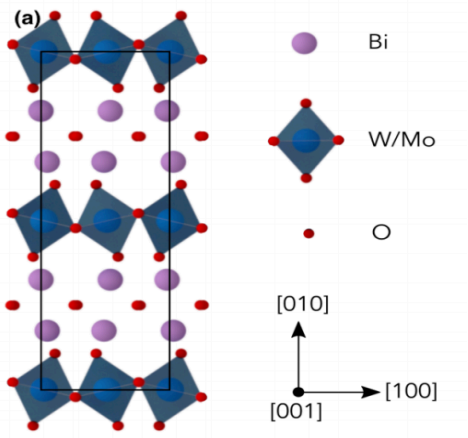

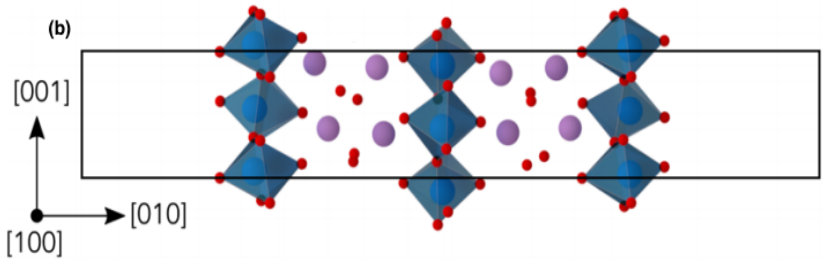

Figure 1.4 (a) Layered structure and (b) slab structure of bulk Bi_2WO_6 and Bi_2MoO_6 compounds[29]

As the bandgaps of Bi_2WO_6 and Bi_2MoO_6 fall nearly in the visible region, they are becoming promising for photocatalytic applications. Nanomaterials of Bi_2MO_6 with a variety of morphologies have been fabricated through hydrothermal or solvothermal method. For example, Zhang et al.[30] reported the synthesis of nanostructured Bi_2WO_6 bipyramids with a large fraction of {100} facets by solvothermal method using ethylene glycol (EG) as solvent, and the formation of "Bi-O" dimer vacancy pairs on the {100} high-energy facets is conductive to the reduction in bandgap and the decrease of recombination of photogenerated electron/hole pairs, significantly improving the photoactivity of Bi_2WO_6 under solar light. Long and co-workers synthesized Bi_2MoO_6 single-crystal nanobelts with dominant {010} facets, which exhibited facet-enhanced photocatalytic performance for the photodegradation of dye pollutants under visible light irradiation as the photo-induced charge carriers were efficiently separated on the low-index facets due to the exposure of more photoactive sites.[31] In addition, hierarchical structures were also explored, such as hierarchical Bi_2MoO_6 spheres *in situ* assembled by monolayer nanosheets with high selectivity for benzyl alcohol oxidation under light irradiation.[32] Besides, some methods are applied to improve the light harvesting of Bi_2MO_6 materials. For instance, a novel carbon quantum dots-modified Bi_2WO_6 ultrathin nanosheets prepared via hydrothermal method demonstrated relatively low recombination rate of photogenerated charge carriers and enhanced full spectrum light utilization toward organic pollutants.[33] Similar to other semiconductor

materials, heterojunction construction and cocatalysts were used to improve the photocatalytic activity of Bi_2MO_6 compounds as well. For example, Cao et al.[34] prepared a novel 2D/2D heterojunction of MXene(Ti_3C_2)/Bi_2WO_6 nanosheets through *in situ* growth of Bi_2WO_6 nanosheets on the surface of Ti_3C_2 ultrathin nanosheets, which held a short charge transport distance and a large contact area, displaying significant improvement on the photocatalytic activity for the reduction of carbon dioxide (CO_2) under simulated solar irradiation.

1.4.3 Bismuth oxyhalide

As V-VI-VII ternary semiconductors, bismuth oxyhalide (BiOX, X=Cl, Br, I) is another category of bismuth-based semiconductors and a new class of promising layered materials for photocatalytic energy conversion and environmental remediation, and its layered crystalline structure is built by interlacing $[Bi_2O_2]^{2+}$ slabs with double slabs of halogen atoms,[35] as shown in Figure 1.5. The intralayer atoms are connected by strong covalent bonding, while a weak van der Waals interaction exists between the interlayers.[36] The inherent internal static electric fields at the interlayer are formed along the crystal orientation perpendicular to the [X] and $[Bi_2O_2]$ layers caused by polarization of related atoms and orbitals,[37] which is beneficial for the separation of photogenerated electron-hole pairs, and this can be used to explain the superior photocatalytic performance of BiOX materials to some degree. According to the density functional theory (DFT) calculations, the valance band maximum is dominated by O 2p states and X np (n=3, 4 and 5 X=Cl, Br and I) states, whereas the conduction band minimum mainly consists of Bi 6p orbitals.[36,38] Meanwhile, this type of bismuth-based materials is also chemically stable, nontoxic and corrosion-resistant.

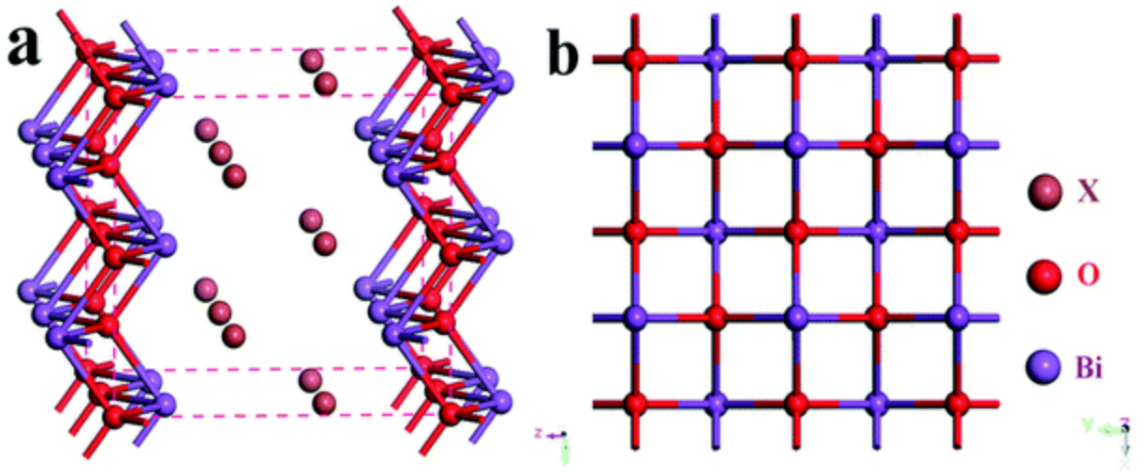

Figure 1.5 Schematic representation for the crystal structure of BiOX (X=Cl, Br, I): (a) Three-dimensional projection and (b) $[Bi_2O_2]^{2+}$ layers along [001] direction[35]

Due to the unique 2D layered structure and suitable bandgap, BiOX-based photocatalysis has become a hot research topic, and various BiOX micro/nanostructures have been synthesized and applied as potential photocatalysts in different fields. For example, Jiang et al. [39] synthesized bismuth oxychloride (BiOCl) single-crystalline nanosheet via a facile hydrothermal route with exposed {001} facets, which exhibited higher activity for direct semiconductor photoexcitation pollutant degradation under UV light. Bismuth oxybromide (BiOBr) photocatalysts with oxygen-deficient defects have been prepared, [40-41] achieving relatively high efficiency of visible-light-driven CO_2 reduction into renewable fuels, during which the oxygen-deficiency-induced defect states could effectively trap photogenerated electrons and thus improve the separation of charge carriers. Hierarchical bismuth oxyiodide (BiOI) microspheres[42] were successfully synthesized by a microwave-assisted solvothermal method, which displayed quite high photocatalytic hydrogen production rate from water splitting via the irradiation of visible light. To further improve the photocatalytic activity of BiOX materials and enable their potential industrial applications, a number of attempts have been made through increasing the light harvesting,

electronic structure tailoring, promoting the separation and transfer of photo-induced electron-hole pairs.

Structural design of BiOX photocatalysts is an effective approach to modify the optical and catalytic properties because of the structure-property correlation. The optical property of one material is related to its underlying electronic and band structure, which could be tuned by doping of foreign atoms or introduction of defects.[43] For instance, BiOCl is a UV light sensitive photocatalyst with no response to visible light, which limits its practical applications in photocatalytic reactions. Wang et al.[44] synthesized cobalt (Co) doped BiOCl nanosheets using a simple hydrothermal method, which formed a doping energy level without changing the layered structure substantially. Most importantly, Co-doping expanded the light absorption region and enhanced separation efficiency of the photogenerated charge carriers, exhibiting a drastically improved photocatalytic activity toward bisphenol A degradation under visible light irradiation. Since BiOX compounds have similar layered structure, atomic arrangement and chemical composition to each other, doping halogen atoms to bismuth oxyhalide is theoretically feasible. Hierarchical nanostructured 3D flowerlike $BiOCl_xBr_{1-x}$ semiconductors[45] were synthesized via a simple procedure at room temperature and demonstrated an excellent photocatalytic activity driven by visible light. Xie et al.[46] prepared a series of $BiOCl_xI_{1-x}$ structures with improved photocatalytic degradation of Rhodamine B by a rapid and cheap solid-state chemical process through the adjustment of the ratio between Cl and I. Facet control is a way to design the structure of BiOX as different crystal facets of semiconductor crystals exhibit different reactivities and surface physical/chemical properties originating from various atomic arrangements and electronic structure. For example, two nanosheet-assembled BiOI microspheres with exposed {110} and {001} facets were prepared respectively, and the one with exposed {110} facets exhibited much

higher photocatalytic activity than that with exposed {001} facets in the visible light excited degradation of bisphenol A.[47]

Constructing plasmonic photocatalysis system by anchoring metals to the surface of semiconductors is another commonly used method to improve light harvesting and to reduce the recombination rate of photo-charges. For example, a series of Ag/BiOI photocatalysts with different Ag contents were prepared by a combination of hydrothermal and photo-deposition methods, and the result revealed that Ag/BiOI composites displayed a much higher photocatalytic activity for degradation of several contaminants than that of pure BiOI under visible light. [48] Bi metal/defective BiOBr hierarchical microspheres were fabricated and exhibited highly enhanced photocatalytic NO oxidation under visible light as a result of synergistic effects of Bi metals and oxygen vacancies.[49] Similarly, Bi-nanowires-deposited BiOCl plasmonic photocatalysts were synthesized by partial reduction of Bi^{3+}, and the Bi/BiOCl with exposed {010} facets demonstrated superior and stable photoactivity under visible light.[50]

Additionally, heterojunction construction is also an effective way to improve the photocatalytic activity of bismuth oxyhalide by decreasing the recombination rate of photogenerated electron-hole pairs. So far, a lot of semiconductors have been coupled with BiOX to form heterojunction structures. For instance, 2D/2D BiOCl/g-C_3N_4[51] ultrathin heterostructure nanosheets demonstrated enhanced visible-light-driven photocatalytic activity in environmental remediation. BiOCl/Bi_2S_3 nano-heterostructures had been prepared through epitaxial growth of Bi_2S_3 nanorods on BiOCl nanosheets via solvothermal treatment,[52] which displayed better visible light absorption and photoelectrochemical performance by influencing the charge separation process. Wang et al.[53] fabricated a novel three-dimensional BiOBr/Bi_2SiO_5 p-n hetero-structured nanocomposite with improved photocatalytic degradation of tetracycline due to

enhancement of the separation efficiency of carriers. Li et al.[54] synthesized $ZnWO_4$/BiOI heterostructure via chemical bath approach under mild conditions, which displayed high photocatalytic activities in degradation of methyl orange under visible light irradiation.

Apart from the commonly used simple BiOX compounds, a series of bismuth oxyhalides with non-stoichiometric ratios, also known as bismuth-rich bismuth oxyhalides (denoted as $Bi_xO_yX_z$, X = Cl, Br and I), such as $Bi_4O_5I_2$[55], Bi_5O_7I[56], $Bi_{12}O_{15}Cl_6$[57], $Bi_{12}O_{17}Cl_2$[58], Bi_3O_4Br[59], $Bi_4O_5Br_2$[60] and $Bi_{24}O_{31}Br_{10}$[61], have been extensively studied in photocatalysis field. Moreover, the layered structure is retained for $Bi_xO_yX_z$ materials, while the charge density of the [Bi-O] layer increased compared with that of double halogen slabs.[62] Theoretically, tuning the ratio of halides in bismuth oxyhalides could modulate the band structure and its bandgap energy by increasing the Bi and O contents and decreasing the X contents in BiOX compounds because of their band structure composition of valance band and conduction band, which represents another promising direction for their photocatalytic activity enhancement.

Among the $Bi_xO_yX_z$ materials, $Bi_{12}O_{17}Cl_2$ is a narrow bandgap semiconductor with a unique layered structure of $Bi_{12}O_{17}^{2+}$ and Cl_2^{2-} slabs.[63] It can absorb visible light and has been applied to photodegrade organic pollutants and selective oxidation.[58,64] However, with a quick charge recombination of photogenerated electron-hole pairs, $Bi_{12}O_{17}Cl_2$ still possesses relatively poor properties for the degradation of pollutants. Effective approaches to advance the photocatalytic performance of $Bi_{12}O_{17}Cl_2$ were introduced by researchers recently, including morphology control, loading noble metals and forming heterojunction structure. For instance, Di et al.[65] designed a $Bi_{12}O_{17}Cl_2$ superfine nanotubes with a bilayer thickness of the tube wall to achieve structural distortion for the creation of surface oxygen defects, which are conducive to the acceleration of carrier migration and promotion of CO_2 activation, and the nanotube structure

boosts the photocatalytic CO_2 reduction. Wang et al.[66] obtained ultrathin $Bi_{12}O_{17}Cl_2$ nanosheets modified with Ag with enhanced visible light absorption and improved separation efficiency under visible light irradiation, resulting in better photocatalytic performance for Rhodamine B decomposition. 2D/2D layered g-C_3N_4/$Bi_{12}O_{17}Cl_2$[67] and carbon-doped carbon nitride/$Bi_{12}O_{17}Cl_2$[68] hybrid materials with matched energy band structure were constructed, and a clearly improved photocatalytic degradation reaction was observed, which can be ascribed to the strong interfacial contact between the C_3N_4 layers and $Bi_{12}O_{17}Cl_2$ sheets with a promoted charge separation efficiency. He et al.[69] prepared a novel 3D flower-like $Bi_{12}O_{17}Cl_2$/β-Bi_2O_3 composite by using a solvothermal-calcining process and evaluated their photocatalytic performance. The as-synthesized hybrid materials possessed favorable band structure, heterojunction structure, relatively high specific surface areas and hierarchical nanostructure, and thus showed improved photocatalytic efficiency for the degradation of a representative alkylphenol. Huang et al.[70] developed a p-n junction BiOI@ $Bi_{12}O_{17}Cl_2$ heterostructure via assembling BiOI onto $Bi_{12}O_{17}Cl_2$, which enabled high exposure of {001} reactive facets of BiOI that resulted in a dramatically strengthened photocatalytic activity toward degradation of multiple industrial contaminants and antibiotics under visible light illumination. In addition, the n-n type bismuth oxychloride phase-junction BiOCl/$Bi_{12}O_{17}Cl_2$[71-72] composites were fabricated, which exhibited enhanced photocatalytic performance under simulated solar light and visible light.

1.4.4 Other bismuth-based compounds

In addition to the abovementioned commonly used bismuth-based materials in photocatalysis field, other bismuth-based semiconductor materials are also applied on various photocatalytic applications, such as Bi_2O_3[73], Bi_2S_3 and $BiPO_4$. Among them, $BiPO_4$ with a wide bandgap can only be excited by UV light and is an excellent UV light photocatalyst, while Bi_2O_3

and Bi_2S_3 can be used as visible light-response photocatalysts. Since Bi_2S_3 has a quite narrow bandgap, it is usually combined with other materials to form heterojunction structure to further improve activity by reducing the recombination rate of photo-induced charge carriers, like WO_3/Bi_2S_3[74]. Similarly, $BiPO_4$ is also coupled with a narrow bandgap semiconductor to achieve synergistic effect, improving the photocatalytic activity under visible light through the separation and transfer of charge carriers between these two semiconductors, such as $BiPO_4$/BiOI composite[75].

1.5 Research objective

Based on the above review, bismuth oxyhalide compounds, including BiOX and $Bi_xO_yX_z$, are comparatively promising 2D layered materials for photocatalytic application in both energy conversion and environmental treatment due to their unique physical and chemical properties, including low cost, nontoxicity, strong oxidation ability, relatively high stability that can stand photo-corrosion, and suitable band structure for utilizing a wide range of light spectrum.

Construction of heterojunction structures by coupling several semiconductor components with appropriate electronic structures has consistently been considered as an effective way to suppress the recombination of photo-induced charge carriers and therefore improve the photocatalytic performance for different applications in the photocatalysis field. Also, the layered structure of bismuth oxyhalide-based materials provides a good two-dimensional platform for the growth of other semiconductors. Herein, in this study, the objective was to form a novel heterojunction-structured photocatalyst by combining bismuth oxyhalide compound with bismuth-rich bismuth oxyhalide compound, more specifically, $BiOBr/Bi_{12}O_{17}Cl_2$, through *in situ* loading of one component onto the other to enhance their photocatalytic activity in water treatment application under visible light or solar light irradiation. Coupling of BiOBr and $Bi_{12}O_{17}Cl_2$

provides a new possibility to further promote the photocatalytic efficiency under solar light or visible light toward several different kinds of refractory organic compounds.

Chapter 2 Experimental Section

2.1 Materials and instruments

Materials used for the experiments are listed in table 2.1, and all reagents were used as received without further purification. The instruments used during the experiments are listed in table 2.2.

Table 2.1 Raw materials and reagents used in experiments

Materials	Vendor	Chemical formula
Bismuth nitrate pentahydrate	Acros	$Bi(NO_3)_3 \cdot 5H_2O$
Sodium chloride	Fisher Scientific	NaCl
Sodium bromide	Alfa Aesar	NaBr
Ethylene glycol	Alfa Aesar	$C_2H_6O_2$
4-Chlorophenol	Acros	C_6H_5ClO
Tetracycline	Alfa Aesar	$C_{22}H_{24}N_2O_8$
Methyl Orange	Acros	$C_{14}H_{14}N_3NaO_3S$
Ammonium oxalate monohydrate	Alfa Aesar	$(COONH_4)_2 \cdot H_2O$
p-Benzoquinone	Alfa Aesar	$C_6H_4O_2$
2-Propanol (Isopropanol)	Alfa Aesar	$(CH_3)_2CHOH$

Table 2.2 Instruments used during synthesis of materials

Instrument	Vendor	Model
Stirring Hotplate	Fisher Scientific	Isotemp
Box furnace	Fisher Scientific	Lindberg/Blue M
Analytical balance	VWR	164-AC
Isotemp Oven	Fisher Scientific	737F
Centrifuge	Fisher Scientific	Sorvall ST-16

2.2 Synthesis of BiOBr/$Bi_{12}O_{17}Cl_2$ photocatalyst

2.2.1 Synthesis of $Bi_{12}O_{17}Cl_2$ layered structure

The layer-structured $Bi_{12}O_{17}Cl_2$ nanomaterial was obtained by a slightly modified solvothermal method[76] followed by calcination at a specific temperature. In a typical synthetic process, 9 mmol of $Bi(NO_3)_3 \cdot 5H_2O$ and 1.5 mmol NaCl used as Bi source and Cl source were dissolved in 50 mL and 20mL ethylene glycol (EG) solution respectively to produce clear solution with the help of ultrasonication at room temperature. Then, NaCl solution was added to $Bi(NO_3)_3$ solution dropwise under continuous stirring to form a transparent mixed solution. After keeping magnetically stirring for another 30 min, the resultant mixture was transferred to a 100 mL teflon-coated autoclave and held at 160℃ for 24 h. After being naturally cooled to room temperature, the precipitates formed in the solution were then collected through centrifugation, and washed with distilled water and ethanol for several times respectively. The products were dried at 60℃ overnight. The final layered $Bi_{12}O_{17}Cl_2$ nanomaterials were obtained after calcination of the above hydrothermal products at 450°C for 1 h at a ramping rate of 5 °C/min.

2.2.2 Fabrication of BiOBr/$Bi_{12}O_{17}Cl_2$ heterojunction composite

The novel heterojunction composite material of $Bi_{12}O_{17}Cl_2$ nanoplates coupled with different amounts of BiOBr (denoted as X-BiOBr/$Bi_{12}O_{17}Cl_2$, X is the mass ratio of BiOBr to $Bi_{12}O_{17}Cl_2$) was prepared by *in situ* deposition-precipitation method. Typically, an appropriate amount of $Bi_{12}O_{17}Cl_2$ materials was dispersed to 25 mL EG under sonication for 20 min and subsequent agitation for 10 min. Then a desired amount of $Bi(NO_3)_3 \cdot 5H_2O$ was added to the above $Bi_{12}O_{17}Cl_2$ suspension with constant stirring. With the assist of sonication, $Bi(NO_3)_3$ was uniformly dissolved in the $Bi_{12}O_{17}Cl_2$ suspension. A solution by dissolving NaBr with same stoichiometric as $Bi(NO_3)_3$ in 25 mL distilled water was added dropwise. Then the mixture was

stirred for another 6 h under dark condition until precipitates were generated. Finally, the obtained BiOBr/$Bi_{12}O_{17}Cl_2$ product was centrifuged and washed with distilled water and ethanol separately and dried at 60℃ overnight. A series of BiOBr/$Bi_{12}O_{17}Cl_2$ composites with different mass proportions (X=60%, 80%, 100%, 125%, 150%) were fabricated using the same method by adjusting the amount of $Bi(NO_3)_3$ and NaBr added. In addition, pure BiOBr materials were also prepared for comparison following an identical method without addition of $Bi_{12}O_{17}Cl_2$.

2.3 Characterization of photocatalysts materials

X-Ray Diffraction (XRD)

The crystal structure of as-prepared samples was characterized at room temperature by using powder XRD on a Bruker D8 Discover X-ray diffractometer with Cu Kα radiation at a scanning speed of 8°min^{-1}. An accelerating voltage of 40 kV and emission current of 40 mA were employed.

Scanning Electron Microscope (SEM)

SEM with energy dispersive X-ray spectroscopy (EDS) was performed on a Hitachi S-4800 FE-SEM machine equipped with a Bruker energy-dispersive system detector, which was used to analyze the topography and morphology of the photocatalysts.

Transmission electron microscopy (TEM)

TEM was carried out on a Hitachi H-9000-NAR instrument to further observe the morphology and microstructure.

Fourier transform infrared (FT-IR)

FT-IR spectra were obtained on a Shimadzu IRTracer-100 spectroscopy to identify functional groups of as-prepared materials.

Brunauer–Emmett–Teller (BET)

Nitrogen adsorption-desorption isotherms and BET surface areas were determined through a Micromeritics ASAP 2020 device, and the pore size distribution was calculated from the Barrett-Joyner-Halenda (BJH) desorption branch.

Diffuse reflectance spectra (DRS)

Ultraviolet visible (UV-vis) DRS spectra were collected through a Shimadzu UV-2600 spectrophotometer using $BaSO_4$ as the reference.

Photoluminescence (PL) spectra

The PL spectra were acquired through a Cary Eclipse fluorescence spectrophotometer.

Electrochemical impedance spectroscopy (EIS)

EIS was carried out on a CHI 600 electrochemical workstation under ambient conditions in a standard three-electrode configuration with the as-prepared samples loaded on a glassy carbon electrode as the working electrode, a platinum wire as the counter electrode and a commercial Ag/AgCl electrode as the reference electrode. 0.1M Na_2SO_4 aqueous solution was used as the electrolyte.

X-ray photoelectron spectroscopy (XPS)

The surface chemical composition and elemental chemical states of samples were studied by XPS using a PerkinElmer PHI 5400 ESCA system equipped with Mg anode as X-ray source.

2.4 Evaluation of photocatalytic activities

The photocatalytic performance of the as-prepared samples was evaluated through the photodegradation of 4-chlorophenol (4-CP) under simulated sunlight irradiation and photodegradation of methyl orange (MO) and tetracycline (TC) under visible light irradiation in a photochemical reactor placed under a light source. The light source was a 300 W Xe arc lamp (Ceaulight, CEL-HXF300) equipped with a detachable 420 nm cut-off filter. During the process

of reaction, the temperature of the reaction system was controlled at a constant value by a circulating cooling device (Figure 2.1).

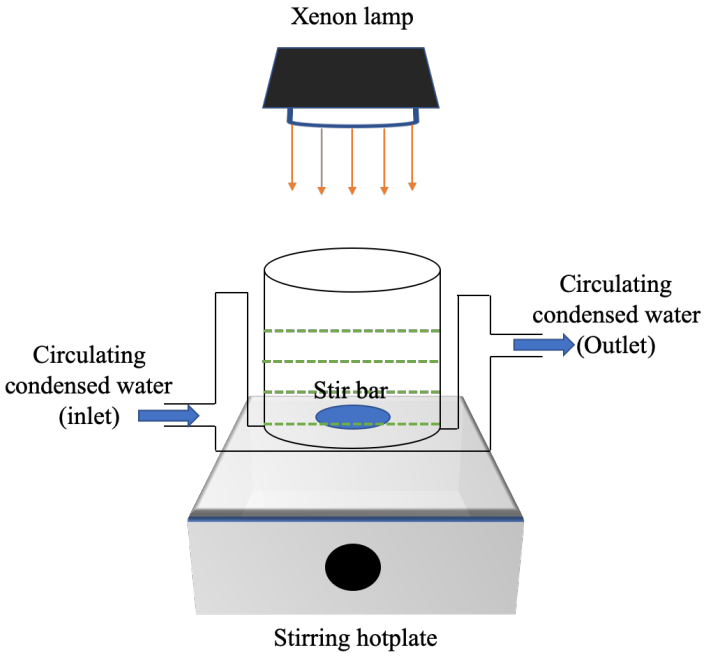

Figure 2.1 Schematic illustration of experimental setup used in photoreaction experiments

In a typical photocatalytic experiment, 25 mg of samples was added to 50 mL of a 4-CP solution (10 mg/L), a TC solution (20 mg/L) or a MO solution (10 mg/L) to obtain an aqueous suspension. Prior to irradiation, the suspension was ultrasonicated for 3 min and stirred in dark for 30 min to achieve the adsorption-desorption equilibrium. During the photocatalytic tests, 2 mL of suspension was sampled at a certain time interval, followed by centrifugation at 11000 rpm for 5 min to remove the photocatalyst materials. The concentration of 4-CP was quantified by a Thermo Ultimate 3000 high performance liquid chromatography (HPLC) equipped with a Thermo Acclaim C18 column and ultraviolet detector at λ=282 nm. A mixture of methanol and water with 0.1% phosphoric acid (70:30, v/v) was applied as the isocratic eluent at a flow rate of 1.0 mL/min. The concentration of MO in the supernatant was determined by means of UV spectrophotometer

(Shimadzu UV-2600) at a wavelength of 464 nm, the characteristic absorption peak of MO. Similarly, the concentration of TC was analyzed using UV spectrophotometer at the maximal absorption wavelength of TC at 358 nm.

The photocatalytic efficiency was calculated using the following equation:

$$\text{Photocatalytic efficiency} = (C_0\text{-}C_t)/C_0 \times 100\% \quad (2.1)$$

where C_0 is the initial concentration of the pollutant, and C_t refers to the pollutant concentration at time t after light irradiation.

Chapter 3 Result and Discussion for $BiOBr/Bi_{12}O_{17}Cl_2$ heterojunction structure

3.1 Introduction

BiOBr and $Bi_{12}O_{17}Cl_2$ are both layered bismuth oxyhalide compounds with narrow bandgaps and high chemical stability, which are of great research interest. However, high recombination rate of photo-induced electron/hole pairs limited their photocatalytic activities. In this work, we successfully coupled $Bi_{12}O_{17}Cl_2$ with BiOBr to construct a novel heterostructured $BiOBr/Bi_{12}O_{17}Cl_2$ composite through a facile and reproducible *in situ* deposition-precipitation method for the first time, where 2D $Bi_{12}O_{17}Cl_2$ acted as the support for the growth of BiOBr nanoplates. The content of BiOBr in this novel composite photocatalyst was optimized. Several different organic compounds were selected to estimate the photocatalytic performance of $BiOBr/Bi_{12}O_{17}Cl_2$ composites, including MO, TC and 4-CP.[77-78] Particularly, 4-CP has been recorded as a priority pollutant by the United States Environmental Protection Agency because of its wide use in the production of herbicides, insecticides and preservatives. Our results showed that the photocatalytic performance of the $BiOBr/Bi_{12}O_{17}Cl_2$ composites was significantly enhanced in comparison to pure BiOBr and $Bi_{12}O_{17}Cl_2$. Various characterization methods were applied to have a better understanding of the physicochemical properties of the as-prepared samples and the relationship between the specific structure and the enhancement of photocatalytic activity. In the meantime, a possible photocatalytic mechanism for the hierarchical $BiOBr/Bi_{12}O_{17}Cl_2$ composite was also proposed. This work provided insight into guiding the design of $BiOBr/Bi_{12}O_{17}Cl_2$ photocatalytic materials and paved the road to the application of $BiOBr/Bi_{12}O_{17}Cl_2$ as a low-cost, efficient and stable photocatalyst in water and wastewater treatment.

3.2 Characterization results of BiOBr/$Bi_{12}O_{17}Cl_2$ composite photocatalysts

3.2.1 XRD patterns

XRD was used to examine the crystal structure of the photocatalyst materials. Figure 3.1 showed the XRD patterns of bare $Bi_{12}O_{17}Cl_2$, BiOBr and the obtained various BiOBr/$Bi_{12}O_{17}Cl_2$ composites with different ratios. For pure $Bi_{12}O_{17}Cl_2$, the diffraction peaks at 23.2°, 24.3°, 26.4°, 29.2°, 30.4°, 32.9°, 45.5°, 47.2°, 54.9° and 56.5° were ascribed to the (111), (113), (115), (117), (0012), (200), (2012), (220), (315) and (317) diffraction planes respectively, which were well indexed to the tetragonal $Bi_{12}O_{17}Cl_2$ (JCPDS no. 37-0702, lattice constants a=b=5.443Å, c=35.200Å).[70, 79] While for the spectra of bare BiOBr, the characteristic diffraction peaks detected at 10.9°, 25.2°, 31.7°, 32.2°, 46.3° and 57.2° were respectively attributed to the (001), (101), (102), (110), (200) and (212) crystal planes, which were in accordance with the tetragonal phase of BiOBr (JCPDS 09-0393).[80] After deposition of BiOBr, the characteristic peaks belong to $Bi_{12}O_{17}Cl_2$ in the BiOBr/$Bi_{12}O_{17}Cl_2$ composites were detected, indicating that loading of BiOBr on $Bi_{12}O_{17}Cl_2$ did not destroy the phase structure of the $Bi_{12}O_{17}Cl_2$ support. With the increase of BiOBr content, the intensities of the characteristic peaks of BiOBr gradually strengthened in the BiOBr/$Bi_{12}O_{17}Cl_2$ composites. The relative intensities of diffraction peaks of $Bi_{12}O_{17}Cl_2$ were decreased, which were probably ascribed to the coverage of BiOBr on the surface of the $Bi_{12}O_{17}Cl_2$ nanoplates.[81] Both XRD patterns of $Bi_{12}O_{17}Cl_2$ and BiOBr can be observed and no impurity peaks were detected in the BiOBr/$Bi_{12}O_{17}Cl_2$ composites, which indicated the successfully synthesis of BiOBr/$Bi_{12}O_{17}Cl_2$ composites.

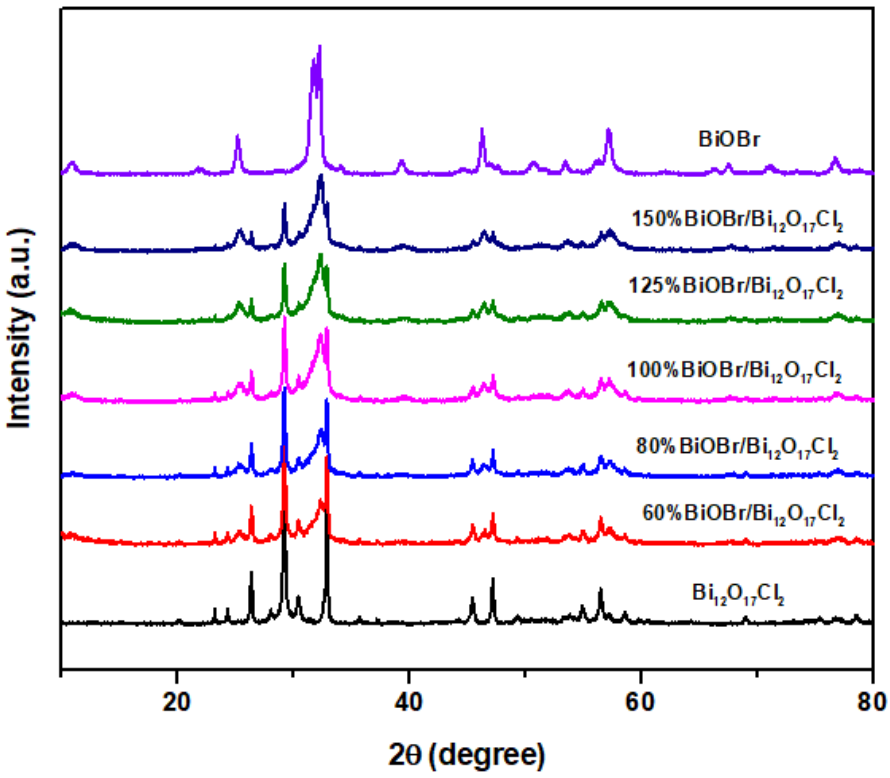

Figure 3.1 XRD patterns of $Bi_{12}O_{17}Cl_2$, BiOBr and BiOBr/$Bi_{12}O_{17}Cl_2$ composites with different mass ratios.

3.2.2 Morphology and microstructures

3.2.2.1 SEM analysis

The morphology and fine microstructure of $Bi_{12}O_{17}Cl_2$, BiOBr and BiOBr/$Bi_{12}O_{17}Cl_2$ composite were revealed by SEM. Figure 3.2(A) illustrated the layered structure of $Bi_{12}O_{17}Cl_2$ with plenty of irregular 2D nanoplates tending to randomly aggregate to large clusters with smooth surfaces exposed, and the relatively large and flat $Bi_{12}O_{17}Cl_2$ 2D nanoplates may provide a good platform for BiOBr to grow on. For pure BiOBr, as shown in Figure 3.2(B), it presented a microsphere structure assembled by lots of nanosheets. After loading BiOBr on the surface of $Bi_{12}O_{17}Cl_2$, the SEM image of BiOBr/$Bi_{12}O_{17}Cl_2$ (X=100%), as displayed in Figure 3.2(C), was different from that of BiOBr and $Bi_{12}O_{17}Cl_2$, and a large portion of BiOBr nanoplates were

vertically and uniformly attached on the surface of $Bi_{12}O_{17}Cl_2$ nanoplates, which not only enabled intimate interfacial interaction between BiOBr and $Bi_{12}O_{17}Cl_2$, but also prevented aggregation of BiOBr nanoplates, posing great effect on the photocatalytic activity. In the meantime, the EDS mapping was applied to determine the distribution of elements on the surface of the 100%-BiOBr/$Bi_{12}O_{17}Cl_2$ composite, as shown in Figure 3.3. All of the involved elements of Bi, O, Cl and Br could be clearly observed, and the homogeneity of the composite was also demonstrated through the uniform distribution of elements, suggesting the formation of the BiOBr/$Bi_{12}O_{17}Cl_2$ composite.

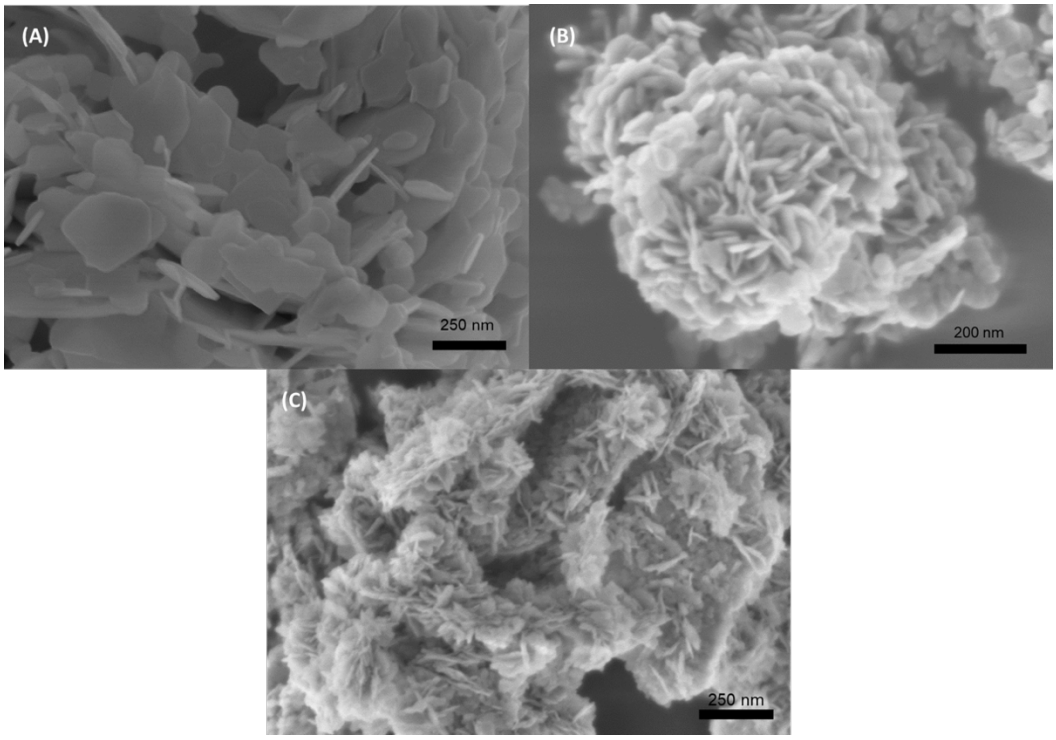

Figure 3.2 SEM images of $Bi_{12}O_{17}Cl_2$ (A), BiOBr (B) and BiOBr/$Bi_{12}O_{17}Cl_2$ composite (X=100%) (C)

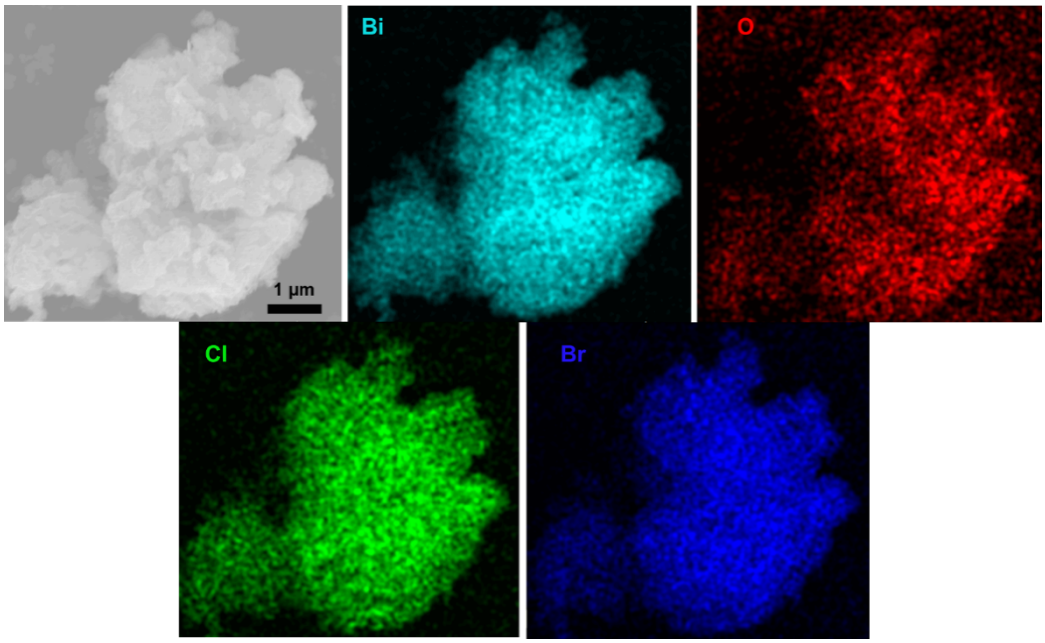

Figure 3.3 EDX images of the BiOBr/$Bi_{12}O_{17}Cl_2$ composite

3.2.2.2 TEM analysis

Further detailed information related to morphology and crystallography of the samples were studied by TEM, as exhibited in Figure 3.4. Notably, the pure $Bi_{12}O_{17}Cl_2$ exhibited irregular thin and flat nanosheet structure as demonstrated in Figure 3.4(A), and pure BiOBr displayed an aggregated cluster composing of a vast of nanoplates with diameters ranging from around 50 to 150 nm (Figure 3.4(B)). Besides, it can be seen that many BiOBr nanoplates were vertically attached onto $Bi_{12}O_{17}Cl_2$ nanosheets through surface-to-surface contact from Figure 3.4(C) of the BiOBr/$Bi_{12}O_{17}Cl_2$ composite. All of these TEM results agreed well with the SEM observations. To better understand the interfacial structure between these two phases, the composite sample was characterized by high-resolution TEM (HRTEM), as shown in Figure 3.4(D). The lattice fringes of 0.271 nm and 0.337 nm were assigned to the interplanar distance of (200) and (115) planes of $Bi_{12}O_{17}Cl_2$, respectively.[68,70,82] Meanwhile, it can be seen that the clear and wide interplanar

d-spacing of about 0.814 nm taken from the side of BiOBr nanoplate, which could be ascribed to the (001) lattice plane of BiOBr.[83] The results indicated the formation of heterojunction structures with intimate interface contact between $Bi_{12}O_{17}Cl_2$ and BiOBr, which would be beneficial for the electron transfer process during photoreactions.

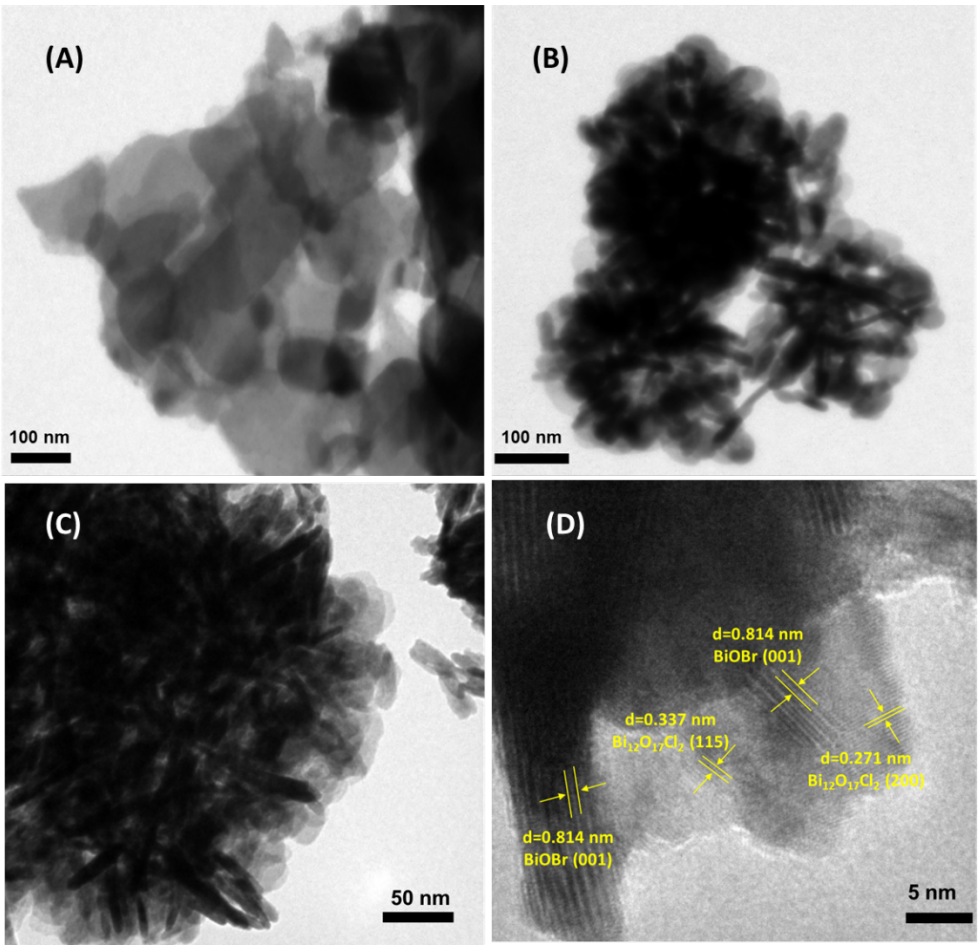

Figure 3.4 TEM images of $Bi_{12}O_{17}Cl_2$ (A), BiOBr (B), BiOBr/$Bi_{12}O_{17}Cl_2$ composite (X=100%) (C) and HRTEM of BiOBr/$Bi_{12}O_{17}Cl_2$ composite (X=100%) (D).

3.2.3 FT-IR analysis

As shown in Figure 3.5, a comparison of the as-prepared BiOBr/$Bi_{12}O_{17}Cl_2$ composites to pure BiOBr and $Bi_{12}O_{17}Cl_2$ in functional groups were researched through using the FT-IR spectra to further characterize the samples. For pure BiOBr, an obvious absorption band appeared at 518

cm^{-1} which can be ascribed to the characteristic symmetrical A_{2u}-type stretching vibrations of Bi-O band[84-85], which became stronger as the content of BiOBr increased. For pure $Bi_{12}O_{17}Cl_2$, the absorption peaks positioned around 460 cm^{-1} and 550 cm^{-1} (centered at nearly 500 cm^{-1}) were assigned to the stretching vibrations of the Bi-O bands in $Bi_{12}O_{17}Cl_2$, while the absorption peak at 846 cm^{-1} can be attributed to the bending vibrations of the O-Bi-O bands.[86-87] The absorption peak at around 1394 cm^{-1} could be assigned to the asymmetric stretching vibration peak of Bi-Cl band in $Bi_{12}O_{17}Cl_2$ structure.[88] As the content of BiOBr increased, its characteristic absorption peak appeared and intensified, while intensities of the characteristic absorption peaks for $Bi_{12}O_{17}Cl_2$ reduced, which was consistent with the result of XRD patterns. Additionally, after forming BiOBr/$Bi_{12}O_{17}Cl_2$ composites, the absorption peak of $Bi_{12}O_{17}Cl_2$ at around 460 cm^{-1} shifted to a slightly higher position, indicating the interfacial interactions caused by the construction of this heterojunction between BiOBr and $Bi_{12}O_{17}Cl_2$, which was probably helpful for the transfer and separation of photoinduced electron-hole pairs as well as the improvement of photocatalytic activities. On the other hand, both the characteristic IR absorption peaks of BiOBr and $Bi_{12}O_{17}Cl_2$ could be observed for the as-made BiOBr/$Bi_{12}O_{17}Cl_2$ composites, further suggesting that the BiOBr/$Bi_{12}O_{17}Cl_2$ photocatalyst materials have been synthesized.

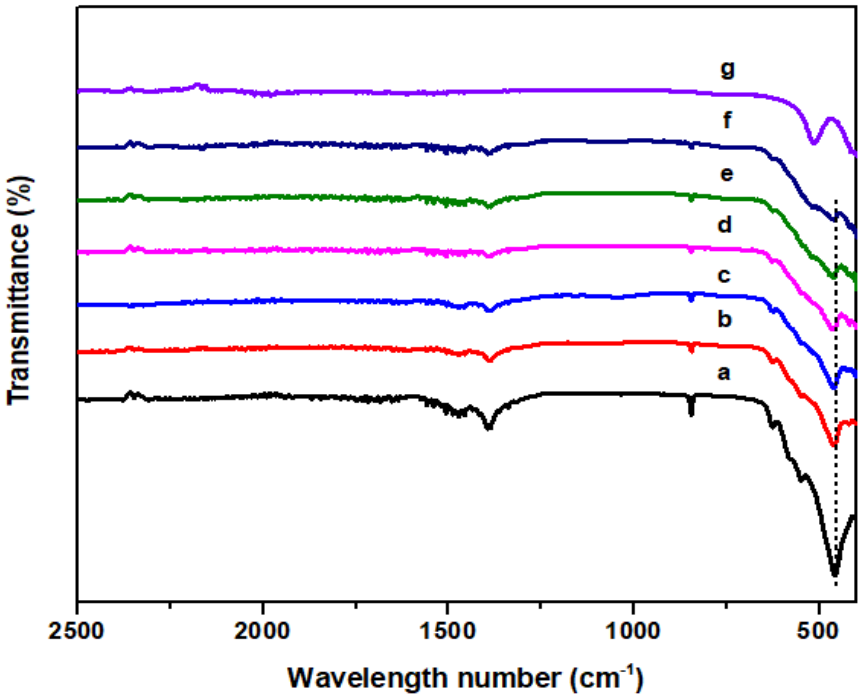

Figure 3.5 FT-IR spectra of $Bi_{12}O_{17}Cl_2$ (a), 60%-BiOBr/$Bi_{12}O_{17}Cl_2$ (b), 80%-BiOBr/ $Bi_{12}O_{17}Cl_2$ (c), 100%-BiOBr/ $Bi_{12}O_{17}Cl_2$ (d), 125%-BiOBr/ $Bi_{12}O_{17}Cl_2$ (e), 150%-BiOBr/$Bi_{12}O_{17}Cl_2$ (f) and BiOBr (g).

3.2.4 XPS analysis

XPS was carried out to further analyze the surface composition and chemical state of the as-synthesized samples. Figure 3.6 revealed the XPS survey spectra of $Bi_{12}O_{17}Cl_2$, BiOBr and 100%-BiOBr/$Bi_{12}O_{17}Cl_2$ and the corresponding Bi 4f, Cl 2p, O 1s and Br 3d high-resolution spectra were illustrated in Fig. 3-7, through which the oxidation states and electronic environment of elements in these samples were analyzed. The survey spectra of these three samples contained adventitious carbon species and other relevant elements to their chemical compositions. In the Bi 4f high-resolution XPS spectra (Figure 3.7(A)), there were two distinct binding energy peaks at 158.7 eV and 164.0 eV for $Bi_{12}O_{17}Cl_2$, which could be respectively ascribed to Bi $4f_{7/2}$ and Bi $4f_{5/2}$ of characteristic Bi^{3+} ions with spin-orbit splitting of 5.3 eV.[89] Likewise, the binding energies of Bi $4f_{7/2}$ and Bi $4f_{5/2}$ were 159.4 eV and 164.7 eV for pure BiOBr in Figure 3.7(A). For Bi 4f of

100%-BiOBr/$Bi_{12}O_{17}Cl_2$, there were two binding energy peaks separately situated at 159.1 eV for Bi $4f_{7/2}$ and 164.4 eV for $4f_{5/2}$, locating between Bi 4f of $Bi_{12}O_{17}Cl_2$ and Bi 4f of BiOBr, which were different from both pure $Bi_{12}O_{17}Cl_2$ and BiOBr, implying the existence of two kinds of chemical states of Bi[71] coming from both BiOBr and $Bi_{12}O_{17}Cl_2$. Figure 3.7(B) exhibited the XPS spectra of Cl 2p for $Bi_{12}O_{17}Cl_2$, which can be divided into two individual peaks with binding energies at 197.6 eV and 199.1 eV that could be attributed to Cl $2p_{3/2}$ and Cl $2p_{1/2}$ of Cl^-, respectively.[82] For 100%-BiOBr/$Bi_{12}O_{17}Cl_2$, however, its binding energy peaks of Cl 2p increased by about 0.3, shifting to 197.9 eV and 199.4 eV, respectively. The Br 3d XPS spectra of BiOBr could be fitted into two peaks located at 68.4 eV and 69.6 eV separately, as displayed in Figure 3.7(C), which were characteristic of Br^- in BiOBr material corresponding to Br $3d_{5/2}$ and Br $3d_{3/2}$, respectively.[90] In comparison to the XPS spectra of Br 3d in BiOBr, the 0.1 eV shifting towards lower binding energy (68.3 eV and 69.5 eV, respectively) was observed in Br 3d spectra for 100%-BiOBr/$Bi_{12}O_{17}Cl_2$. In terms of the high-resolution XPS spectra for O 1s of pure $Bi_{12}O_{17}Cl_2$ shown in Figure 3.7(D), it could be deconvoluted into two kinds of binding energies located at 532.3 eV and 530.0 eV, which could be assigned to adsorbed surface hydroxyl groups and the lattice oxygen (Bi-O), respectively.[91-92] Similarity, two peaks at 532.3 eV and 530.6 eV were observed in O 1s XPS spectra for BiOBr. However, the binding energy peak ascribed to the lattice Bi-O in the 100%-BiOBr/$Bi_{12}O_{17}Cl_2$ composite shifted to 530.2 eV, which was consistent with the result of Bi 4f XPS spectra. All above analysis suggested the presence of interaction between $Bi_{12}O_{17}Cl_2$ and BiOBr in the BiOBr/$Bi_{12}O_{17}Cl_2$ sample, which may slightly affect the chemical environment of individual elements. As a result, the chemical compositions and valance states revealed in the XPS spectra was coincident with the XRD, FT-IR and TEM

results and further confirmed the successful construction of BiOBr/$Bi_{12}O_{17}Cl_2$ heterojunction composite by deposition-precipitation process.

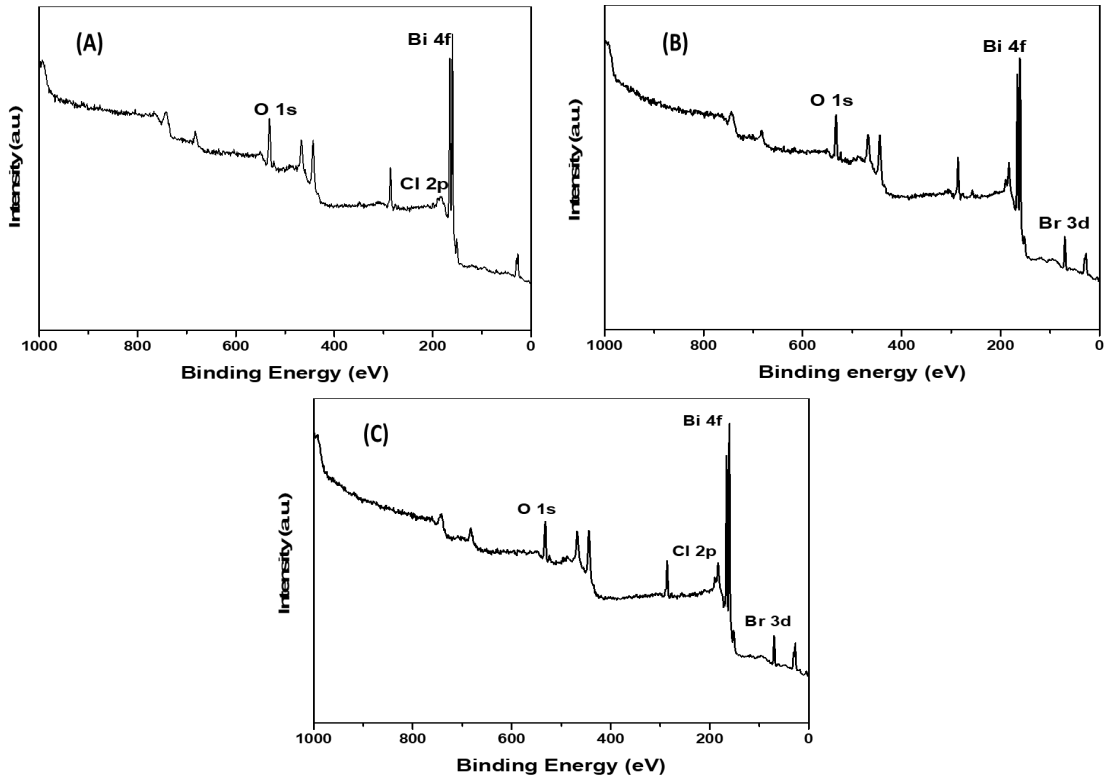

Figure 3.6 XPS survey spectra of $Bi_{12}O_{17}Cl_2$ (A), BiOBr (B) and BiOBr/$Bi_{12}O_{17}Cl_2$ composite (X=100%) (C)

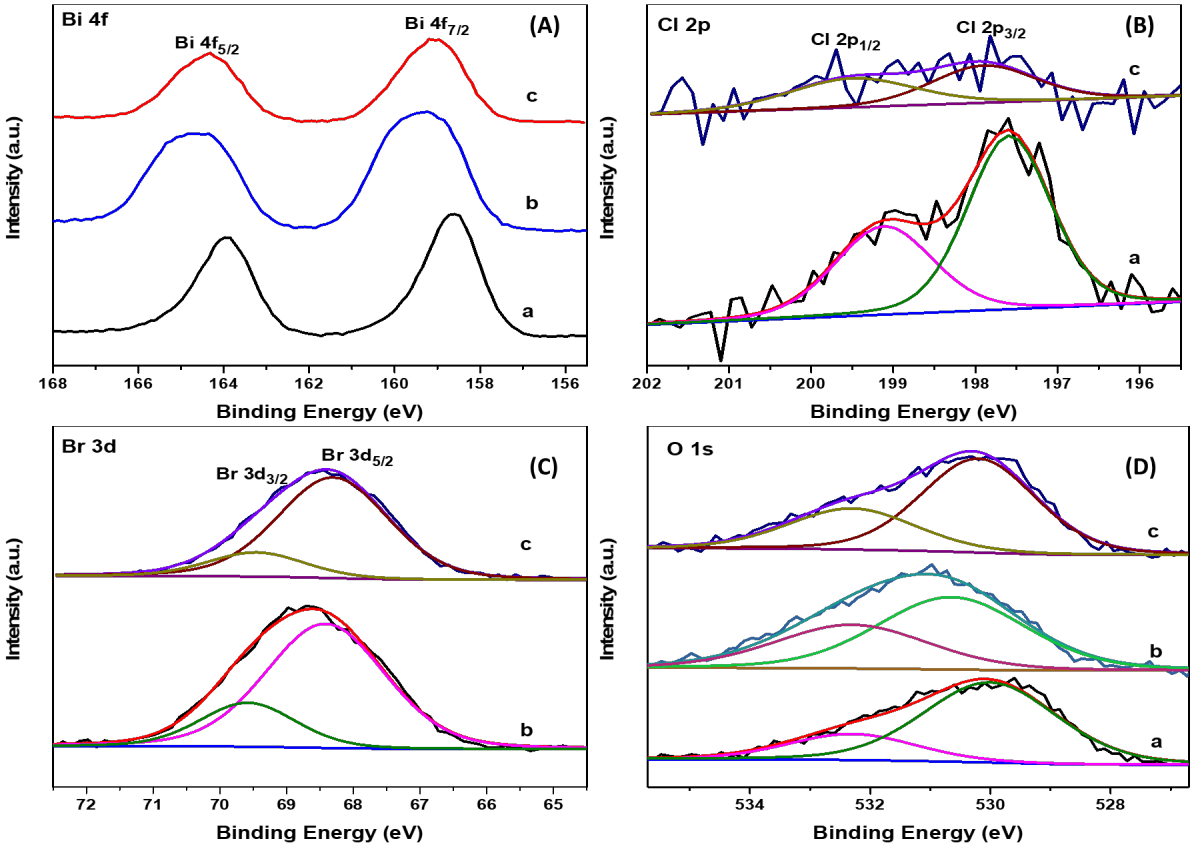

Figure 3.7 XPS spectra of Bi 4f (A), Cl 2p (B), Br 3d (C) and O 1s (D) for $Bi_{12}O_{17}Cl_2$ (a), BiOBr (b) and BiOBr/ $Bi_{12}O_{17}Cl_2$ composite (X=100%) (c).

3.2.5 BET analysis

Photocatalytic reaction is a kind of interfacial reaction, so the contact of organic compounds with the surface of photocatalyst materials, which provides active sites, is a critical step to initiate the photocatalytic decomposition reaction. Thus, a larger specific surface area would be helpful for the adsorption of organic compound. The BET surface areas and porous structure of the as-prepared samples were investigated through the N_2 adsorption-desorption isotherms, as presented in Figure 3.8. The N_2 adsorption-desorption isotherms curves of pure $Bi_{12}O_{17}Cl_2$, BiOBr and 100%-BiOBr/$Bi_{12}O_{17}Cl_2$ can be indexed to type IV with a typical H3 hysteresis loop observed at relatively high P/P_0 between 0.7 and 1.0, which suggested the presence

of mesoporous structure[93]. The H3 hysteresis loop could probably be resulted from the aggregation of the nanosheets with slit-like pores[94], which was consistent with the SEM results. In addition, the corresponding pore size distribution curves calculated from the desorption branch were displayed in the insets of Figure 3.8, which confirmed that these materials contain a large portion of mesopores (2-50 nm). Table 3.1 listed the specific surface areas of the as-prepared samples through N_2 adsorption-desorption analysis (BET method) and their corresponding average pore diameters, all of which were in the mesoporous range. It can be clearly seen that the combination of BiOBr with $Bi_{12}O_{17}Cl_2$ could increase the surface area of the BiOBr/$Bi_{12}O_{17}Cl_2$ composites and all the BiOBr/$Bi_{12}O_{17}Cl_2$ composite materials have much larger surface areas than that of pure $Bi_{12}O_{12}Cl_2$. Moreover, the specific surface area first increased and then decreased with raising the amount of BiOBr in the composite, which may indicate that the existence of appropriate portion of $Bi_{12}O_{17}Cl_2$ nanoplates as support could prevent the congregate of BiOBr nanoplates. The composite of 100%-BiOBr/$Bi_{12}O_{17}Cl_2$ had the largest specific surface area among all samples, which was conducive to supply of more active sites, the adsorption of organic contaminants around active sites and then maximize the photocatalytic performance.[95] Therefore, the relatively high specific surface area was one of the factors that influenced the photocatalytic performance of BiOBr/$Bi_{12}O_{17}Cl_2$ hybrid composites.

Table 3.1 BET surface areas and average pore sizes of the as-prepared samples

Sample	S_{BET} (m^2/g)	Average pore diameter (nm)
$Bi_{12}O_{17}Cl_2$	9.4523	16.7
60%BiOBr/$Bi_{12}O_{17}Cl_2$	30.2761	14.3
80%BiOBr/$Bi_{12}O_{17}Cl_2$	37.1264	12.6
100%BiOBr/$Bi_{12}O_{17}Cl_2$	48.1407	11.9
125%BiOBr/$Bi_{12}O_{17}Cl_2$	43.0496	13.7
150%BiOBr/$Bi_{12}O_{17}Cl_2$	40.4553	12.4
BiOBr	34.2868	18.1

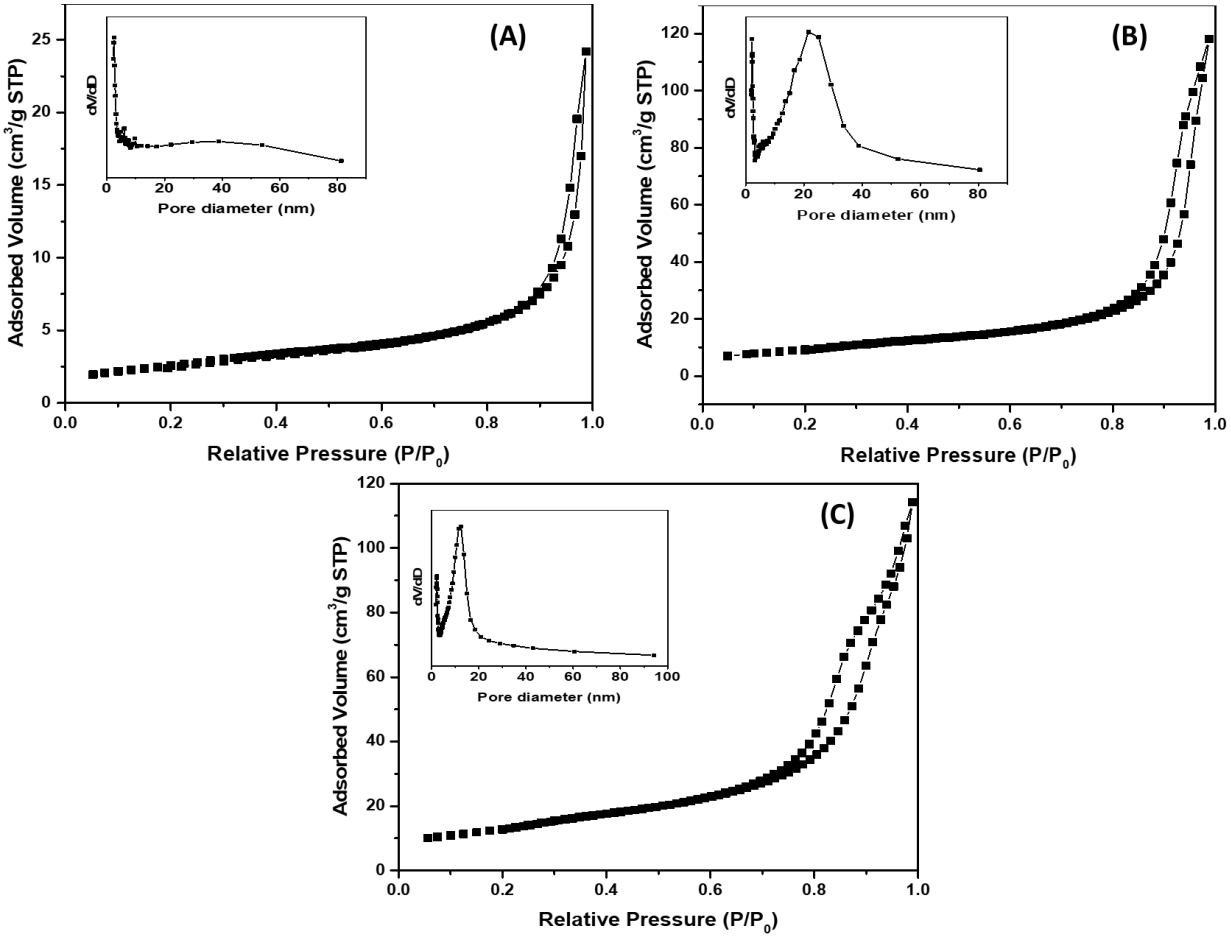

Figure 3.8 Nitrogen adsorption-desorption isotherms and corresponding pore size distribution curves (inset) of pure $Bi_{12}O_{17}Cl_2$ (A), BiOBr (B) and BiOBr/$Bi_{12}O_{17}Cl_2$ (X=100%) composite (C).

3.2.6 Optical absorption properties

In photocatalysis field, optical absorption property is an important factor to consider when designing novel photocatalytic materials, and it may play a critical role in determining photocatalytic performance since all photochemical processes are initiated by light absorption. The optical properties and electronic structures of as-prepared samples were measured through UV-vis UV-vis DRS to determine their light absorption ability. Figure 3.9(A) showed the UV-vis DRS spectra of $Bi_{12}O_{17}Cl_2$, BiOBr and BiOBr/$Bi_{12}O_{17}Cl_2$ composites. It was clearly seen that the photo-response of $Bi_{12}O_{17}Cl_2$ ranged from UV light region to visible light region with the absorption edge around 530 nm, a characteristic band caused by the transition from valance band to the conduction band, indicating the satisfactory light response capacity and suitable band structure. While for BiOBr, it had an absorption edge ending up to approximately 430 nm absorbing the relatively short-wavelength light, which was attributed to electron transition from the valance band (hybridized O 2p and Br 4p orbit) to the conduction band (Bi 6p orbital).[96] After hybridization, the BiOBr/$Bi_{12}O_{17}Cl_2$ composites exhibited enhanced absorption intensity in the visible light region as the content of $Bi_{12}O_{17}Cl_2$ increased, which was in agreement with the colors of corresponding samples changing from white of BiOBr to pale yellow, and finally to bright yellow of $Bi_{12}O_{17}Cl_2$. The composite that can absorb more light would be useful to generate photoinduced charges and promote the photoactivity.

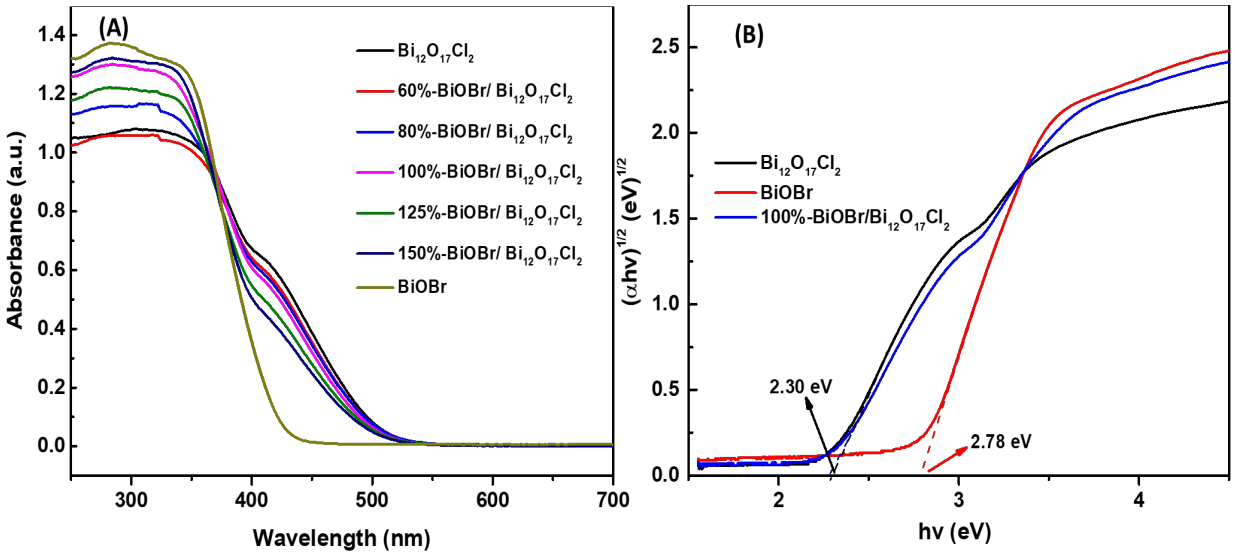

Figure 3.9 (A) UV-vis diffuse reflectance spectra of $Bi_{12}O_{17}Cl_2$, BiOBr and BiOBr/$Bi_{12}O_{17}Cl_2$ composites with different ratios; (B) Plots of $(\alpha hv)^{1/2}$ vs photo energy (hv) for $Bi_{12}O_{17}Cl_2$, BiOBr and BiOBr/$Bi_{12}O_{17}Cl_2$ (X=100%) composite.

It is well known that the bandgap energy of a semiconductor can be evaluated by the following equation:

$$\boldsymbol{\alpha hv = A\,(hv - E_g)^{n/2}} \qquad \boldsymbol{(3.1)}$$

where α, h, v, Eg and A are the absorption coefficient, Planck's constant, light frequency, bandgap energy and a constant, respectively. Also, the value of n is determined by the type of optical transition of a semiconductor, that is, n=1 for direct transition and n=4 for indirect transition. It has been previously reported that both of $Bi_{12}O_{17}Cl_2$ and BiOBr were classified as indirect transition[53,68], and thus their bandgap energies were respectively estimated to be 2.30 eV and 2.78 eV through the Tauc Plots of the as-synthesized samples from which the bandgap of the semiconductor was governed by the linear region. Although bandgap mainly reflected the optical property of a single semiconductor, the bandgap energy of 100%-BiOBr/$Bi_{12}O_{17}Cl_2$ was calculated as about 2.28 eV using a similar fashion, as displayed in Figure 3.9(B). Compared to $Bi_{12}O_{17}Cl_2$ and BiOBr, the bandgap energy of the composite became slightly smaller after forming

heterojunction structure, and the narrowed bandgap may be beneficial to improving the ability of light harvest especially in the visible light region.

3.3 Photocatalytic performance and stability of BiOBr/$Bi_{12}O_{17}Cl_2$ composites

3.3.1 Study of photocatalytic performance

The photocatalytic activities of the as-prepared samples were evaluated by the degradation of 4-CP under simulated solar light irradiation. Figure 3.10(A) showed the photodegradation of 4-CP as a function of irradiation time over different photocatalysts. A blank test in the absence of the photocatalyst confirmed that the self-photolysis of 4-CP was negligible after irradiation for 120 min. Bare BiOBr and $Bi_{12}O_{17}Cl_2$ achieved moderate photodegradation efficiencies of 74% and 67% after 120 min, respectively, proving that 4-CP was decomposed in the presence of photocatalysts. Compared to pristine BiOBr and $Bi_{12}O_{17}Cl_2$, all BiOBr/ $Bi_{12}O_{17}Cl_2$ composites exhibited enhanced photocatalytic performance for degradation of 4-CP under the same condition. In particular, the content of BiOBr in the composite played a crucial role in the photocatalytic activity, and the photocatalytic efficiency of the composite increased initially as the loading amount of BiOBr raised. When the mass ratio between BiOBr and $Bi_{12}O_{17}Cl_2$ reached 100% (i.e., 100%-BiOBr/$Bi_{12}O_{17}Cl_2$), the highest photocatalytic activity was achieved that approximately 95% of 4-CP was photodegraded even within 90 min. Besides, the photocatalytic activity of the corresponding mechanical mixture of BiOBr and $Bi_{12}O_{17}Cl_2$ with a 1:1 mass ratio was also researched, and its photocatalytic performance for degradation of 4-CP under identical condition was much lower than that of the obtained 100%-BiOBr/$Bi_{12}O_{17}Cl_2$ composite through deposition-precipitation method, suggesting the presence of heterojunction through intimate interfacial contact between BiOBr and $Bi_{12}O_{17}Cl_2$ in the composite material, which would be favorable for

the separation of photo-induced charges. However, further increasing the amount of BiOBr in the composite led to a decrease of photocatalytic activity toward degradation of 4-CP, which may due to the fact that the composite materials became agglomerated with too much BiOBr and the partial active sites on the surface of $Bi_{12}O_{17}Cl_2$ thus were covered by excess BiOBr.[97] The excess BiOBr might also probably act as recombination centers for electron-hole pairs and hinder photo absorption as well.[53,98] As a result, 100%-BiOBr/$Bi_{12}O_{17}Cl_2$ was the best candidate among all samples under the same condition that provided a maximal photocatalytic activity. These results revealed that the synergistic effect between BiOBr and $Bi_{12}O_{17}Cl_2$ had an imperative impact on the improvement of photocatalytic performance.

Generally, the photocatalytic decomposition of organic compounds over semiconductor photocatalysts follows the pseudo-first-order kinetics, so the degradation kinetics of 4-CP were investigated by fitting the experimental data to the following pseudo first-order kinetics equation[99]:

$$-\ln\left(\frac{c}{c_0}\right) = kt \quad (3.2)$$

where c is the concentration of reactant, t is the reaction time and k is the apparent rate constant. Figure 3.10(B) displayed the corresponding linear relationship based on Equation 3.2 and the resulting rate constant k was given in Figure 3.10(C). The as-synthesized 100%-BiOBr/$Bi_{12}O_{17}Cl_2$ composite showed an excellent photodegradation efficiency of 4-CP with a k value of 0.0362 min^{-1}, which was approximately 4.07 times higher of that of single $Bi_{12}O_{17}Cl_2$ (0.0089 min^{-1}) and 3.23 times higher than that of pure BiOBr (0.0112 min^{-1}), and it was larger than other BiOBr/$Bi_{12}O_{17}Cl_2$ composites with different ratios as well. In contrast to the 100%-BiOBr/$Bi_{12}O_{17}Cl_2$, the corresponding mechanically mixed sample also exhibited lower rate constant, suggesting that the

construction of a heterostructure of BiOBr/$Bi_{12}O_{17}Cl_2$ could be an efficient way to enhance the photocatalytic activities.

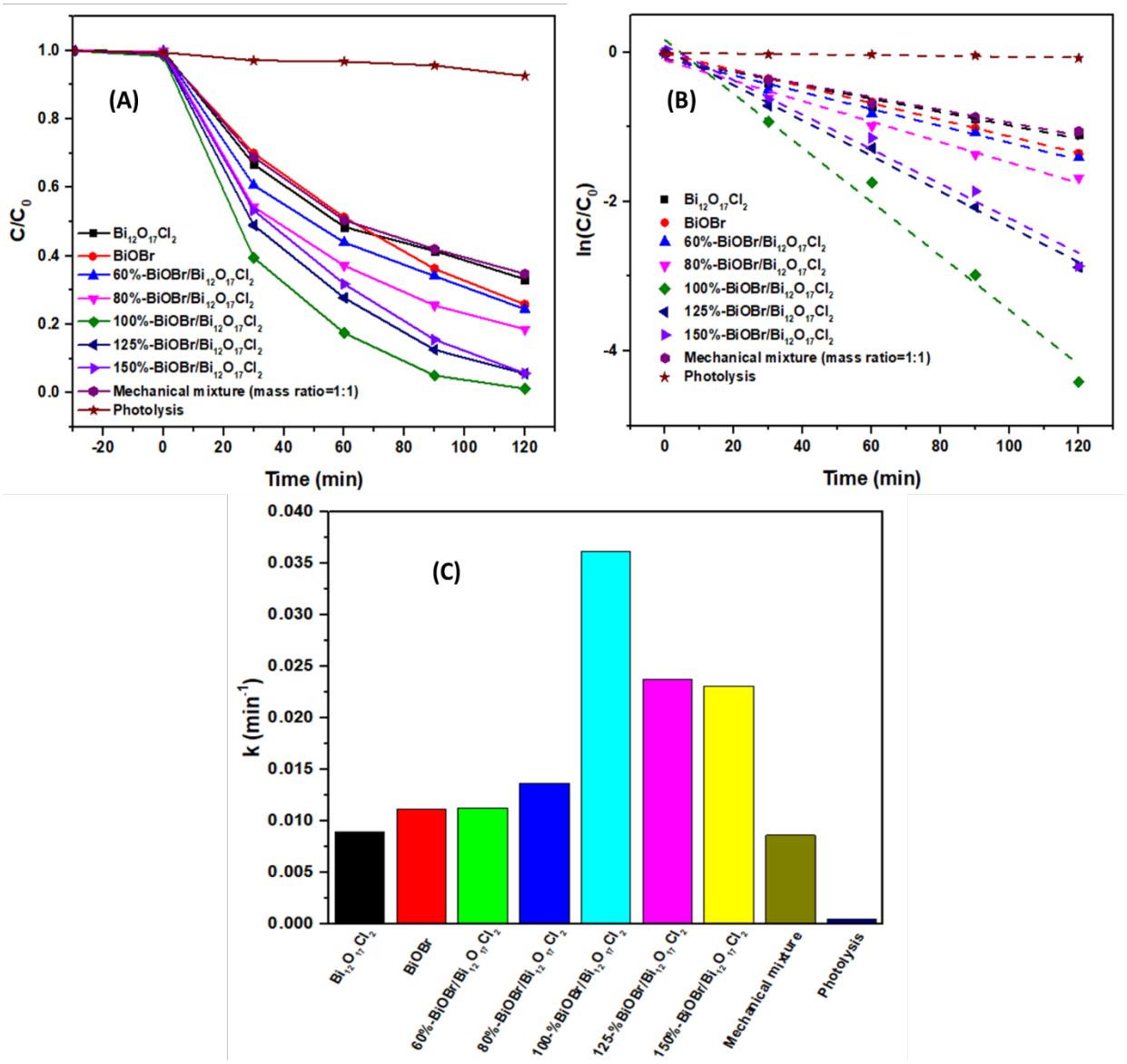

Figure 3.10 Photocatalytic performance for the degradation of 4-CP (A) under simulated solar light and the corresponding kinetics curves over as-prepared catalysts (B) and apparent rate constants over a sprepared photocatalysts (C) under simulated solar light

To further confirm the general application of 100%-BiOBr/$Bi_{12}O_{17}Cl_2$ composite photocatalyst, another two typical pharmaceutical and industrial contaminants, TC and MO, were

adopted to be the target pollutants under the irradiation of visible light (λ>420 nm). Figure 3.11(A) and Figure 3.11(B) exhibited the comparison results of BiOBr, $Bi_{12}O_{17}Cl_2$ and 100%-BiOBr/$Bi_{12}O_{17}Cl_2$ composite for the decomposition of TC and MO, respectively. It was clearly to observe that the 100%-BiOBr/$Bi_{12}O_{17}Cl_2$ composite material showed better photocatalytic degradation of both TC and MO than bare BiOBr and $Bi_{12}O_{17}Cl_2$ under the illumination of visible light, and about 91% of initial TC was photodegraded within 40 min while nearly 95% of initial MO was degraded within 30 min. These results demonstrated that the BiOBr/$Bi_{12}O_{17}Cl_2$ heterostructures possessed excellent photocatalytic ability over a wide range of light spectrum, including the irradiation of solar light and visible light, which may hold great potentials for practical application in environmental remediation.

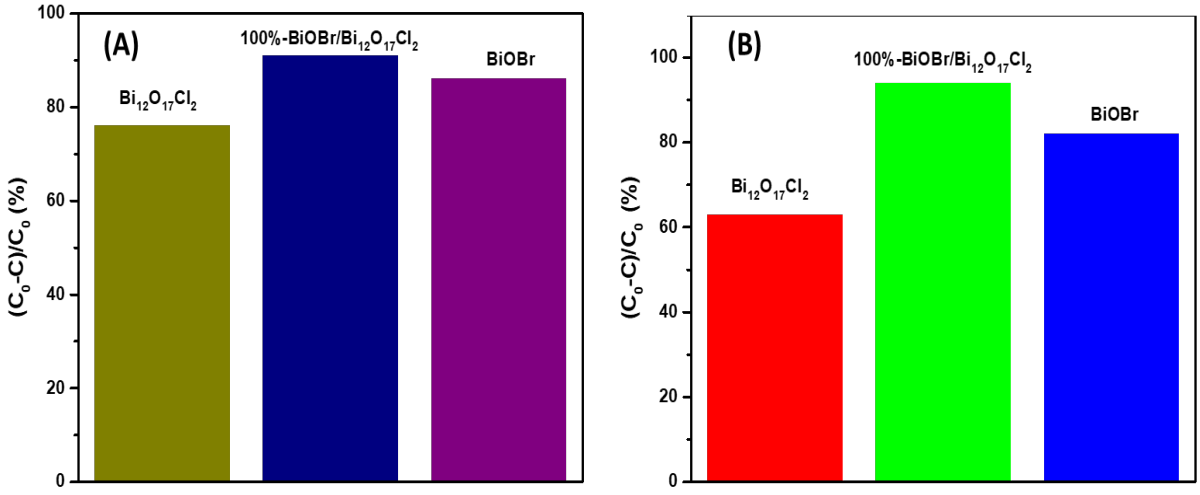

Figure 3.11 Photocatalytic performance for the degradation of TC (A) within 40 min and MO (B) within 30 min under visible light irradiation

3.3.2 Stability analysis of the photocatalyst

From the perspective of practical application, it is crucial to evaluate the stability and reusability of photocatalyst materials. Hence, the stability of the 100%-BiOBr/$Bi_{12}O_{17}Cl_2$

photocatalyst was assessed via the cycling experiments of photocatalytic degradation of 4-CP under simulated solar light irradiation. Three consecutive cycles of photodegradation for 4-CP were carried out by collecting and reusing the photocatalyst under the same condition as mentioned above, and the result was presented in Figure 3.12. After three cycles of photocatalytic reaction, the 100%-BiOBr/$Bi_{12}O_{17}Cl_2$ composite still possessed a relatively high photocatalytic efficiency of around 90% 4-CP photodegradation in 120 min, indicating the high stability of BiOBr/$Bi_{12}O_{17}Cl_2$ catalysts. Compared with the photocatalytic efficiency of the first cycle, the slight decrease may be owing to the weight loss of the photocatalyst powders during the recycling process[81,84].

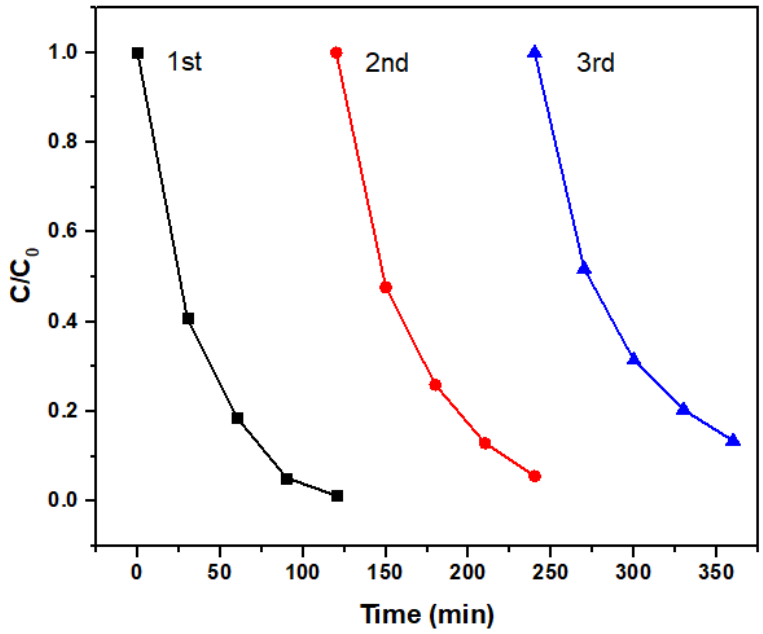

Figure 3.12 Recycling test of 100%-BiOBr/$Bi_{12}O_{17}Cl_2$ for the photodegradation of 4-CP under simulated solar light

3.4 The possible mechanism of the enhanced photocatalytic activity

It is well known that the PL spectroscopy can reflect the migration transfer and separation efficiency of photogenerated electron-hole pairs that directly impact the photocatalytic performance of semiconductors. Specifically, the strength of PL emission intensity is positively proportional to the recombination of excited photoinduced charges; in another word, high intensity of PL emission spectra usually suggests high recombination rate.[79,100] PL spectra of the as-synthesized samples, including BiOBr, $Bi_{12}O_{17}Cl_2$ and 100%-BiOBr/$Bi_{12}O_{17}Cl_2$, were recorded (Figure 3.13 (A)). The pure $Bi_{12}O_{17}Cl_2$ and BiOBr displayed relatively strong PL intensities, implying the lower photo-induced charges separation efficiency. Notably, the PL intensity of BiOBr/$Bi_{12}O_{17}Cl_2$ system decreased significantly compared to those of BiOBr and $Bi_{12}O_{17}Cl_2$ and thus had the lowest PL response, indicating that the BiOBr/$Bi_{12}O_{17}Cl_2$ composite had lower recombination rate of photoinduced electrons and holes after fabrication of heterojunction structure. Result was consistent with the highest photocatalytic activity of the BiOBr/$Bi_{12}O_{17}Cl_2$ composite for the degradation of 4-CP.

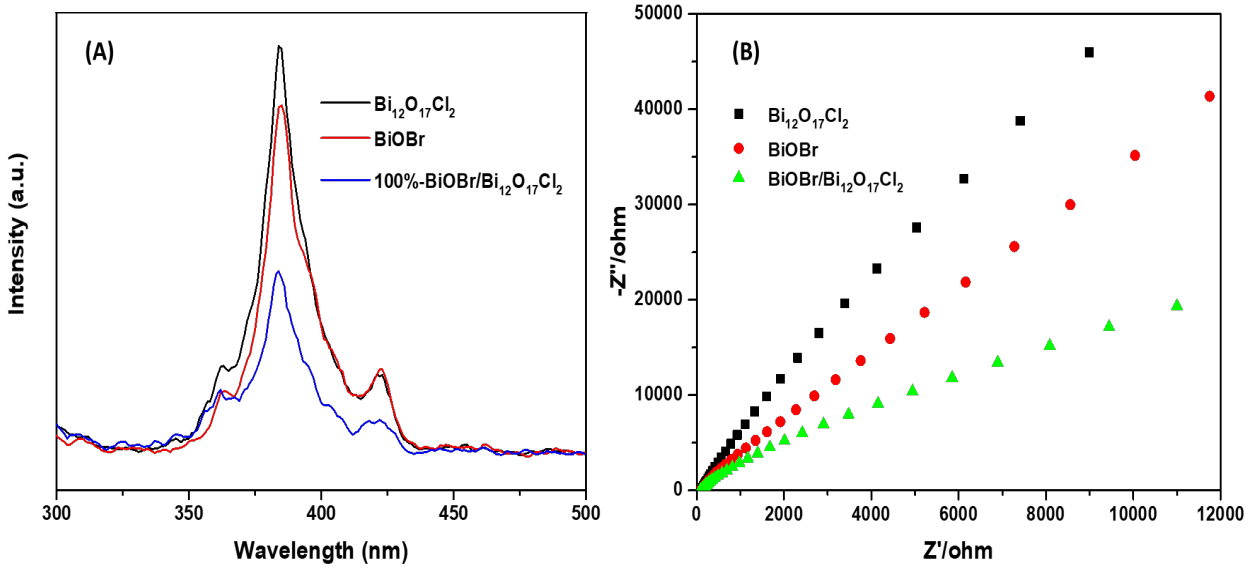

Figure 3.13 (A) Photoluminescence (PL) spectra and (B) Nyquist impedance plots of $Bi_{12}O_{17}Cl_2$, BiOBr and BiOBr/$Bi_{12}O_{17}Cl_2$ composite (X=100%)

EIS is another useful technique to evaluate the interfacial properties between the electrode and electrolyte, such as conductivity and charge transport efficiency. To further verify the efficient separation of carriers, the EIS of BiOBr, $Bi_{12}O_{17}Cl_2$ and 100%-BiOBr/$Bi_{12}O_{17}Cl_2$ was measured, as depicted in Figure 3.13(B). The BiOBr/$Bi_{12}O_{17}Cl_2$ composite exhibited an obvious smaller arc radius in the EIS Nynquist plots in comparison to pristine BiOBr and $Bi_{12}O_{17}Cl_2$, suggesting a smaller interfacial resistance between electrode and electrolyte, and a higher efficiency of charge transfer on the surface, which may be instructive to the reduction for the recombination of electron-hole pairs.[101] Together with the PL spectra and EIS measurements, it could be inferred that the existence of strong interfacial interaction between BiOBr and $Bi_{12}O_{17}Cl_2$ in the heterojunction structures may be beneficial for the separation of electron-hole pairs and thus inhibit the recombination of photoinduced charge carriers, resulting in the enhancement of photocatalytic activities of the as-prepared composite materials.

3.5 Study of photocatalytic reaction mechanism

3.5.1 Exploration of active species during photoreaction

To validate the photocatalytic active species and get insights into the photocatalytic reaction mechanism for the photodegradation process of the BiOBr/$Bi_{12}O_{17}Cl_2$ composite, the trapping experiments for the composite were conducted to determine the main reactive species by adding various scavengers. In this study, isopropanol (IPA), benzoquinone (BQ) and ammonium oxalate (AO) were selected as scavengers of hydroxyl radical (·OH), superoxide radical ($\cdot O_2^-$) and holes (h^+), respectively.[66,102] As presented in Figure 3.14, when BQ or AO was used as scavengers, the photodegradation efficiency of 4-CP was greatly suppressed in the case of 100%-BiOBr/$Bi_{12}O_{17}Cl_2$ compared to that without scavengers, suggesting that $\cdot O_2^-$ and h^+ were likely to

be the main active species that participated in the photocatalytic reaction. While after addition of IPA, the photocatalytic activity of the composite slightly decreased compared to that without scavenger, indicating that ·OH may not be the main active specie during the photodegradation process. Therefore, both $\cdot O_2^-$ and the holes should be the dominant active species that contribute to the photodegradation of 4-CP under simulated solar light, while ·OH plays a minor role in the photocatalytic reaction.

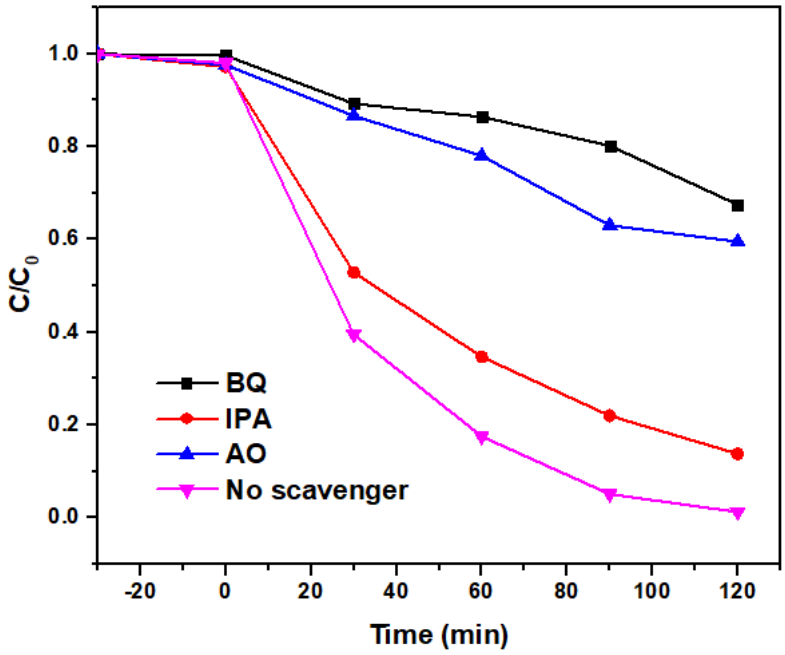

Figure 3.14 Effects of various scavengers on the photocatalytic activity of 100%-BiOBr/$Bi_{12}O_{17}Cl_2$ composite toward degradation of 4-CP under simulated solar light

3.5.2 Proposed photocatalytic reaction mechanism

The relatively high photocatalytic performance of the BiOBr/$Bi_{12}O_{17}Cl_2$ depended on its photoinduced charge carrier generation and subsequent separation, which was probably related to the energy bands and nanostructures. The heterojunction comprising of two semiconductors with suitable band structures may be advantageous to the separation of charge carriers. Based on the

UV-vis DRS analysis, the bandgaps of $Bi_{12}O_{17}Cl_2$ nanoplates and BiOBr were approximately 2.30 eV and 2.78 eV, respectively. To better explain the photocatalytic mechanism and the enhanced photoactivity of BiOBr/$Bi_{12}O_{17}Cl_2$ hybrid composite, the relative positions of valence band maximum for samples were measured by XPS valence spectra. As exhibited in Figure 3.15, the valence band maximum of $Bi_{12}O_{17}Cl_2$ and BiOBr located respectively at about 1.45 eV and 2.17 eV, which were similar to that previous reports,[65,103-104] and the BiOBr nanoplates displayed a more positive location that of $Bi_{12}O_{17}Cl_2$ nanoplates. Consequently, it was reasonable to infer that their corresponding conduction band minimum was respectively –0.85 eV and -0.61 eV for $Bi_{12}O_{17}Cl_2$ and BiOBr, according to the following equation:

$$\boldsymbol{E_{CB} = E_{VB} - E_g} \qquad \boldsymbol{(3.3)}$$

where E_{CB} and E_{VB} are the conduction band position and valance band position, respectively. It was obviously to see that $Bi_{12}O_{17}Cl_2$ and BiOBr in the composites had complementary potentials of valance band and conduction band, and a well-matched band structure between two kinds of semiconductors could in turn effectively separate the photoinduced electron-hole pairs.

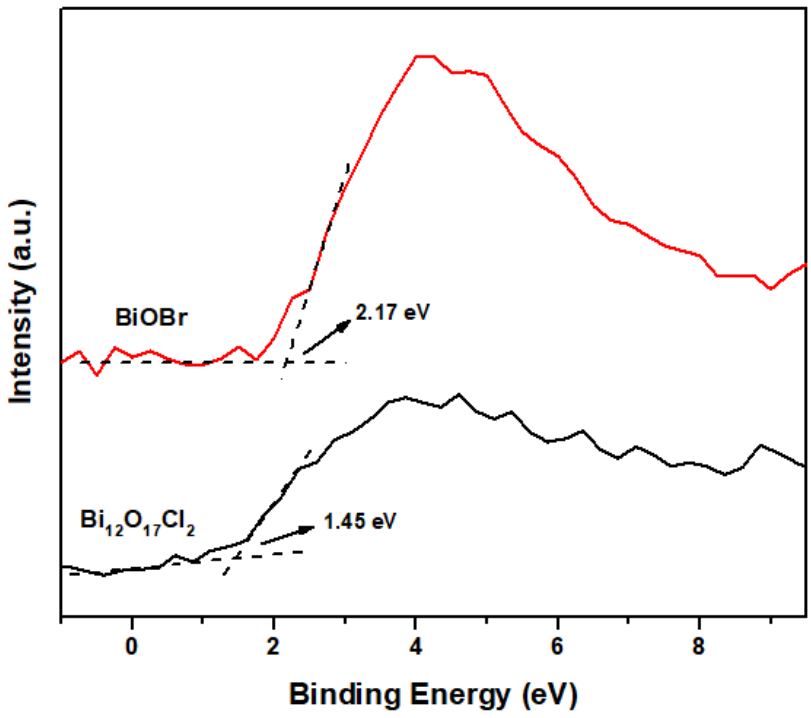

Figure 3.15 The VB XPS spectra for $Bi_{12}O_{17}Cl_2$ and BiOBr

In general, based on the experimental results, a proposed photocatalytic mechanism for photodegradation of organic pollutants over BiOBr/$Bi_{12}O_{17}Cl_2$ hybrid composites was illustrated in Figure 3.16. Both BiOBr and $Bi_{12}O_{17}Cl_2$ could be excited and generate the electrons (e^-) and holes under light irradiation. The photoinduced charge carriers of bare BiOBr or $Bi_{12}O_{17}Cl_2$ were likely to recombine quickly, causing relatively low photocatalytic activity. Whereas, for the BiOBr/$Bi_{12}O_{17}Cl_2$ heterojunctions, the photoexcited electrons of $Bi_{12}O_{17}Cl_2$ in the conduction band can be transferred to the conduction band of BiOBr due to the more negative conduction band position of $Bi_{12}O_{17}Cl_2$. At the same time, the holes produced in the valence band of BiOBr could be migrated to the valance band of $Bi_{12}O_{17}Cl_2$ as the valence band potential of $Bi_{12}O_{17}Cl_2$ was lower than that of BiOBr. This charge transfer effectively suppressed the recombination of photoinduced charges, resulting in more charge carriers to participate in the photoreaction. The

released electrons could be easily trapped by surface adsorbed oxygen (O_2) of the composite to yield superoxide ($\cdot O_2^-$) radicals since the conduction band potential of BiOBr (-0.61 eV) was more negative than the redox potential of E^0 ($O_2/\cdot O_2^-$) (-0.33 eV vs. NHE)[58,105], and then react with organic compounds. However, the photogenerated holes cannot oxidize ambient OH^-/H_2O to produce ·OH due to the fact that the valence band potentials of BiOBr and $Bi_{12}O_{17}Cl_2$ were more negative compared to the redox potential of $OH^-/\cdot OH$ (2.38 eV vs. NHE)[58,106]. Instead, the holes in the valence band could directly oxidize the organic contaminants into small molecules. Additionally, a small part of $\cdot O_2^-$ may react with H^+/H_2O and produce H_2O_2, which may be further excited by electrons to yield ·OH radicals.[107-108] In this route, it might explain the reason that ·OH radicals had limited impact on the photodegradation efficiency of organic compounds, and the obtained main active species (holes and $\cdot O_2^-$) could photodegraded organic compounds into small intermediates or directly into end products (like carbon dioxide or water). Therefore, the interaction between BiOBr and $Bi_{12}O_{17}Cl_2$ in the composite may promote the separation of charge carriers during the photoreaction process, leading to the improvement of photocatalytic performance. The following reactions possibly depicted the feasible reaction steps involved in the process of photodegradation:

$$BiOBr/Bi_{12}O_{17}Cl_2 + h\nu \rightarrow BiOBr/Bi_{12}O_{17}Cl_2\ (e_{CB}^- + h_{VB}^+) \quad (3.4)$$

$$BiOBr/Bi_{12}O_{17}Cl_2\ (e_{CB}^- + h_{VB}^+) \rightarrow BiOBr(e^-)/Bi_{12}O_{17}Cl_2(h^+) \quad (3.5)$$

$$e^- + O_2 \rightarrow \cdot O_2^- \quad (3.6)$$

$$\cdot O_2^- + \cdot O_2^- + 2H^+(\text{ or } H_2O) \rightarrow H_2O_2 + O_2 + (2OH^-) \quad (3.7)$$

$$H_2O_2 + e^- \rightarrow \cdot OH + OH^- \quad (3.8)$$

$$\cdot OH + \text{organic compound} \rightarrow \text{photodegradation} \quad (3.9)$$

$$\cdot O_2^- + \text{organic compounds} \rightarrow CO_2 + H_2O + \text{other products} \quad (3.10)$$

$$h^+ + \text{organic compounds} \rightarrow CO_2 + H_2O + \text{other products} \quad (3.11)$$

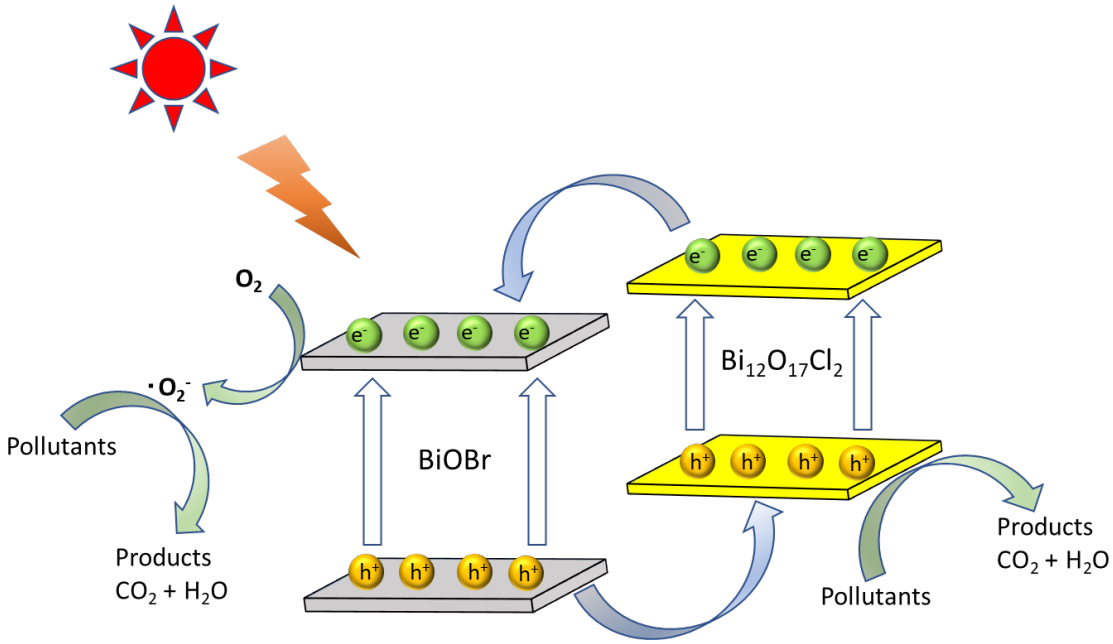

Figure 3.16 Schematic illustration of possible photo-induced electron-hole pairs separation-transport process under light illumination and photodegradation mechanism over BiOBr/$Bi_{12}O_{17}Cl_2$ composite.

Chapter 4 Conclusion and Perspectives

In summary, a novel BiOBr/$Bi_{12}O_{17}Cl_2$ heterojunction composite, for the first time, had been successfully fabricated through a simple chemical precipitation method by *in situ* loading of BiOBr nanoplates on the surface of $Bi_{12}O_{17}Cl_2$ layers. A series of characterization tools were applied to investigate the properties of the novel photocatalytic materials, including XRD for crystal structures, SEM and TEM for morphologies and microstructures, FT-IR for surface functional groups, DRS analysis for optical properties, N_2 adsorption-desorption isotherms for specific surface area and pore size, and XPS for surface composition and chemical states. Compared to pristine BiOBr and $Bi_{12}O_{17}Cl_2$, the as-obtained BiOBr/$Bi_{12}O_{17}Cl_2$ composites exhibited better photocatalytic performance toward degradation of multiple organic compounds under wide-range light irradiation and kept relatively good recyclability during the photodegradation process. The ratio of BiOBr to $Bi_{12}O_{17}Cl_2$ could be easily controlled and had great influence on the corresponding photocatalytic properties, among which 100%-BiOBr/$Bi_{12}O_{17}Cl_2$ was the most effective catalyst for 4-CP photodegradation. The enhancement of photocatalytic activity could be primarily ascribed to the increased separation efficiency of photogenerated electron-hole pairs at the surface of BiOBr and $Bi_{12}O_{17}Cl_2$ caused by their matched band structure, extended light absorption range, as well as increased specific surface area. Moreover, the BiOBr/$Bi_{12}O_{17}Cl_2$ composite displayed relatively good stability through several consecutive recycling tests, making it a promising photocatalyst in practical application. In addition, PL spectroscopy and EIS confirmed the promoted separation and inhibited recombination of photoinduced charges in the heterostructure. Moreover, the results of trapping experiments indicated that the superoxide radicals ($\cdot O_2^-$) and photogenerated holes (h^+) were main active species

for the photodegradation of 4-CP. At last, a possible photocatalytic mechanism was proposed based on the results observed in the experiments.

To have a better understanding of the photocatalytic mechanism of the heterojunction structure and its applications in photocatalysis field, future research may be dedicated to the following directions.

(1) All characterizations in this work did not involve *in situ* study. *In situ* characterization may help understand the reaction mechanism during the photoreaction, and thus future research can focus on *in situ* investigation of the reaction occurred on the surface of the heterojunction composite under the irradiation of light.

(2) In this work, several organic compounds were selected as target pollutants to evaluate the photocatalytic activities of the catalysts individually. Nevertheless, the real water and wastewater can be far more complex. So, experiments under complex water matrices relevant to water and wastewater treatment should be explored in the future.

(3) It may be worth exploring new synthesis method to fabricate heterojunction composite materials with advanced structure, like ultrathin nanosheet with exposed highly reactive facets, to further improve the photocatalytic performance.

(4) Given the band structures and layered morphologies of the bismuth oxyhalides, the photocatalytic performance toward selective oxidation of organic compounds and CO_2 reduction can be explored to expand the scope of application in photocatalysis field.

The present work sheds light on the rational design and development of more efficient and stable photocatalysts via a facile method at room temperature, and the resulting products will have far-reaching applications in solving environmental and energy issues with the development of improved photocatalytic technologies.

References

[1] N. Yahya, F. Aziz, N. A. Jamaludin, M. A. Mutalib, A. F. Ismail, W. N. W. Salleh, J. Jaafar, N. Yusof and N. A. Ludin. A review of integrated photocatalyst adsorbents for wastewater treatment. Journal of Environmental Chemical Engineering, 2018, 6, 7411-7425.

[2] A. Fujishima and K. Honda. Electrochemical Photolysis of Water at a Semiconductor Electrode. Nature, 1972, 238, 37-38.

[3] T. S. Jamil, H. Roland, H. Michael and J. U. Repke. Homogeneous photocatalytic processes for degradation of some endocrine disturbing chemicals under UV irradiation. Journal of Water Process Engineering, 2017, 18, 159-168.

[4] L. Clarizia, D. Russo, I. Di Somma, R. Marotta and R. Andreozzi. Homogeneous photo-Fenton processes at near neutral pH: A review. Applied Catalysis B: Environmental, 2017, 209, 358-371.

[5] K. Shimura and H. Yoshida. Heterogeneous photocatalytic hydrogen production from water and biomass derivatives. Energy Environ. Sci., 2011, 4, 2467-2481.

[6] K. M. Lee, C. W. Lai, K. S. Ngai and J. C. Juan. Recent developments of zinc oxide based photocatalyst in water treatment technology: A review. Water Research, 2016, 88, 428-448.

[7] D. Kim, K. K. Sakimoto, D. Hong and P. D. Yang, Artificial Photosynthesis for Sustainable Fuel and Chemical Production, Angew. Chem. Int. Ed., 2015, 54, 3259-3266.

[8] S. Malato, P. Fernández-Ibáñez, M. I. Maldonado, J. Blanco and W. Gernjak. Decontamination and disinfection of water by solar photocatalysis: Recent overview and trends. Catalysis Today, 2019, 147, 1-59.

[9] Q. P. Lu, Y. F. Yu, Q. L. Ma, B. Chen and H. Zhang, 2D Transition-Metal-Dichalcogenide-Nanosheet-Based Composites for Photocatalytic and Electrocatalytic Hydrogen Evolution Reactions. Adv. Mater., 2016, 28, 1917-1933.

[10] H. L. Wang, L. S. Zhang, Z. G. Chen, J. Q. Hu, S. J. Li, Z. H. Wang, J. S. Liu and X. C. Wang. Semiconductor heterojunction photocatalysts: design, construction, and photocatalytic performances. Chem. Soc. Rev., 2014, 43, 5234-5244.

[11] A. L. Linsebigler, G. Q. Lu and J. T. Yates, Jr. Photocatalysis on TiO_2 Surfaces: Principles, Mechanisms, and Selected Results. Chem. Rev., 1995, 95, 735-758.

[12] B. Jalvo, M. Faraldos, A. Bahamonde and R. Rosal. Antimicrobial and antibiofilm efficacy of self-cleaning surfaces functionalized by TiO_2 photocatalytic nanoparticles against Staphylococcus aureus and Pseudomonas putida. Journal of Hazardous Materials, 2017, 340,160-170.

[13] T. Paik, M. Cargnello, T. R. Gordon, S. Zhang, H. Yun, J. D. Lee, H. Y. Woo, S. J. Oh, C. R. Kagan, P. Fornasiero and C. B. Murray. Photocatalytic Hydrogen Evolution from Substoichiometric Colloidal WO_{3-x} Nanowires. ACS Energy Lett., 2018, 3, 1904-1910.

[14] N. Tian, Z. Li, D. Y. Xu, Y. Li, W. C. Peng, G. L. Zhang, F. B. Zhang and X. B. Fan. Utilization of MoS_2 Nanosheets To Enhance the Photocatalytic Activity of ZnO for the Aerobic Oxidation of Benzyl Halides under Visible Light. Ind. Eng. Chem. Res., 2016, 55, 8726-8732.

[15] M. F. Kuehnel, K. L. Orchard, K. E. Dalle and E. Reisner. Selective Photocatalytic CO_2 Reduction in Water through Anchoring of a Molecular Ni Catalyst on CdS Nanocrystals. J. Am. Chem. Soc., 2017, 139, 7217-7223.

[16] G. D. Yang, Z. Jiang, H. H. Shi, T. C. Xiao and Z. F. Yan. Preparation of highly visible-light active N-doped TiO_2 photocatalyst. J.Mater.Chem., 2010, 20, 5301-5309.

[17] M. S. Zhu, C. Y. Zhai, L. Q. Qiu, C. Lu, A. S. Paton, Y. K. Du and M. C. Goh. New Method to Synthesize S-Doped TiO_2 with Stable and Highly Efficient Photocatalytic Performance under Indoor Sunlight Irradiation. ACS Sustainable Chem. Eng., 2015, 3, 3123-3129.

[18] H. Chaker, L. Chérif-Aouali, S. Khaoulani, A. Bengueddach and S. Fourmentin. Photocatalytic degradation of methyl orange and real wastewater by silver doped mesoporous TiO_2 catalysts. Journal of Photochemistry and Photobiology A: Chemistry, 2016, 318, 142-149.

[19] S. Y. Pu, R. X. Zhu, H. Ma, D. L. Deng, X. J. Pei, F. Qi and W. Chu. Facile in-situ design strategy to disperse TiO_2 nanoparticles on graphene for the enhanced photocatalytic degradation of rhodamine 6G. Applied Catalysis B: Environmental, 2017, 218, 208-219.

[20] C. X. Li, Z. R. Lou, Y. C. Yang, Y. C. Wang, Y. F. Lu, Z. Z. Ye and L. P. Zhu. Hollowsphere Nanoheterojunction of g-C_3N_4@TiO_2 with High Visible Light Photocatalytic Property. Langmuir, 2019, 35, 779-786.

[21] S. S. M. Bhat and H. W. Jang. Recent Advancesin Bismuth-Based Nanomaterials for Photoelectrochemical Water Splitting. ChemSusChem, 2017, 10, 3001-3018.

[22] A. Malathi, J. Madhavan, M. Ashokkumar and P. Arunachalam. A review on $BiVO_4$ photocatalyst: Activity enhancement methods for solar photocatalytic applications. Applied Catalysis A, General, 2018, 555, 47-74.

[23] Z. Y. Zhao, Z. S. Li and Z. G. Zou, Electronic structure and optical properties of monoclinic clinobisvanite $BiVO_4$. Phys. Chem. Chem. Phys., 2011, 13, 4746-4753.

[24] J. Q. Hu, H. C. He, X. Zhou, Z. S. Li, Q. Shen, W. J. Luo, A. Alsaedi, T. Hayat, Y. Zhou and Z. G. Zou. $BiVO_4$ tubular structures: oxygen defect-rich and largely exposed reactive {010} facets synergistically boost photocatalytic water oxidation and the selective N=N coupling reaction of 5-amino-1H-tetrazole. Chem. Commun., 2019, 55, 5635-5638.

[25] C. W. Dong, S. Y. Lu, S. Y. Yao, R. Ge, Z. D. Wang, Z. Wang, P. F. An, Y. Liu, B. Yang and H. Zhang. Colloidal Synthesis of Ultrathin Monoclinic $BiVO_4$ Nanosheets for Z-Scheme Overall Water Splitting under Visible Light. ACS Catal., 2018, 8, 8649-8658.

[26] R. G. Li, F. X. Zhang, D. E. Wang, J. X. Yang, M. R. Li, J. Zhu, X. Zhou, H. X. Han and C. Li. Spatial separation of photogenerated electrons and holes among {010} and {110} crystal facets of $BiVO_4$. Nat. Comm., 2013, 4, 1432.

[27] F. Q. Zhou, J. C. Fan, Q. J. Xu and Y. L. Min. $BiVO_4$ nanowires decorated with CdS nanoparticles as Z-scheme photocatalyst with enhanced H_2 generation. Applied Catalysis B: Environmental, 2017, 201, 77-83.

[28] S. M. Sun and W. Z. Wang. Advanced chemical compositions and nanoarchitectures of bismuth based complex oxides for solar photocatalytic application. RSC Adv., 2014, 4, 47136-47152.

[29] Q. Campbell, D. Fisher and I. Dabo. Voltage-dependent reconstruction of layered Bi_2WO_6 and Bi_2MoO_6 photocatalysts and its influence on charge separation for water splitting. Phys. Rev. Materials, 2019, 3, 015404.

[30] G. Zhang, Z. Y. Hu, M. Sun, Y. Liu, L. M. Liu, H. J. Liu, C.-P. Huang, J. H. Qu and J. H. Li. Formation of Bi_2WO_6 Bipyramids with Vacancy Pairs for Enhanced Solar-Driven Photoactivity. Adv. Funct. Mater., 2015, 25, 3726-3734.

[31] J. L. Long, S. C. Wang, H. J. Chang, B. Z. Zhao, B. T. Liu, Y. G. Zhou, W. Wei, X. X. Wang, L. Huang and W. Huang. Bi_2MoO_6 Nanobelts for Crystal Facet-Enhanced Photocatalysis. Small, 2014, 10, 2791-2795.

[32] K. Q. Jing, W. Ma, Y. H. Ren, J. H. Xiong, B. B. Guo, Y. J. Song, S. J. Liang and L. Wu. Hierarchical Bi_2MoO_6 spheres in situ assembled by monolayer nanosheets toward photocatalytic selective oxidation of benzyl alcohol. Applied Catalysis B: Environmental, 2019,243, 10-18.

[33] J. J. Wang, L. Tang, G. M. Zeng, Y. C. Deng, H. R. Dong, Y. N. Liu, L. L. Wang, B. Peng, C. Zhang and F. Chen. 0D/2D interface engineering of carbon quantum dots modified Bi_2WO_6 ultrathin nanosheets with enhanced photoactivity for full spectrum light utilization and mechanism insight. Applied Catalysis B: Environmental, 2018, 222, 115-123.

[34] S. W. Cao, B. J. Shen, T. Tong, J. W. Fu and J. G. Yu. 2D/2D Heterojunction of Ultrathin MXene/Bi_2WO_6 Nanosheets for Improved Photocatalytic CO_2 Reduction. Adv. Funct. Mater., 2018, 28, 1800136.

[35] L. Cai, G. Q. Zhang, Y. F. Zhang and Y. Wei. Mediation of band structure for $BiOBr_xI_{1-x}$ hierarchical microspheres of multiple defects with enhanced visible-light photocatalytic activity. CrystEngComm, 2018, 20, 3647-3656.

[36] J. Di, J. X. Xia, H. M. Li, S. J. Guo and S. Dai. Bismuth oxyhalide layered materials for energy and environmental applications. Nano Energy, 2017, 4, 172-192.

[37] J. Li, Y. Yu and L. Z. Zhang. Bismuth oxyhalide nanomaterials: layered structures meet photocatalysis. Nanoscale, 2014, 6, 8473-8488.

[38] T. Li, X. C. Zhang, C. M. Zhang, R. Li, J. X. Liu, R. Lv, H. Zhang, P. D. Han, C. F. Fan and Z. F. Zheng. Theoretical insights into photo-induced electron transfer at BiOX (X = F, Cl, Br, I) (001) surfaces and interfaces. Phys. Chem. Chem. Phys., 2019, 21, 868-875.

[39] J. Jiang, K. Zhao, X. Y. Xiao, and L. Z. Zhang. Synthesis and Facet-Dependent Photoreactivity of BiOCl Single Crystalline Nanosheets. J. Am. Chem. Soc. 2012, 134, 4473-4476.

[40] J. Wu, X. D. Li, W. Shi, P. Q. Ling, Y. F. Sun, X. C. Jiao, S. Gao, L. Liang, J. Q. Xu, W. S. Yan, C. M. Wang and Y. Xie. Efficient Visible-Light-Driven CO_2 Reduction Mediated by Defect-Engineered BiOBr Atomic Layers. Angew. Chem. Int. Ed. 2018, 57, 8719-8723.

[41] X. Y. Kong, W. P. C. Lee, W.-J. Ong, S.-P. Chai and A. R. Mohamed. Oxygen-Deficient BiOBr as a Highly Stable Photocatalyst for Efficient CO_2 Reduction into Renewable Carbon-Neutral Fuels. ChemCatChem, 2016, 8, 3074-3081

[42] G.-J. Lee, Y.-C. Zheng and J. J. Wu. Fabrication of hierarchical bismuth oxyhalides (BiOX, X = Cl, Br, I) materials and application of photocatalytic hydrogen production from water splitting. Catalysis Today, 2018, 307, 197-204.

[43] H. F. Cheng, B. B. Huan and Y. Dai. Engineering BiOX (X= Cl, Br, I) nanostructures for highly efficient photocatalytic applications. Nanoscale, 2014, 6, 2009-2026.

[44] C. Y. Wang, Y. J. Zhang, W. K. Wang, D. N. Pei, G. X. Huang, J. J. Chen, X. Zhang and H. Q. Yu. Enhanced photocatalytic degradation of bisphenol A by Co-doped BiOCl nanosheets under visible light irradiation. Applied Catalysis B: Environmental, 2018, 221, 320-328.

[45] H. Gnayem and Y. Sasson. Hierarchical Nanostructured 3D Flowerlike $BiOCl_xBr_{1-x}$ Semiconductors with Exceptional Visible Light Photocatalytic Activity. ACS Catal., 2013, 3, 186-191.

[46] J. Xie, Y. L. Cao, D. Z. Jia and Y. Z. Li. Dahlia-shaped $BiOCl_xI_{1-x}$ structures prepared by a facile solid-state method: Evidence and mechanism of improved photocatalytic degradation of rhodamine B dye. Journal of Colloid and Interface Science, 2017, 503, 115-123.

[47] M. L. Pan, H. J. Zhang, G. D. Gao, L. Liu and W. Chen. Facet-Dependent Catalytic Activity of Nanosheet-Assembled Bismuth Oxyiodide Microspheres in Degradation of Bisphenol A. Environ. Sci. Technol. 2015, 49, 6240-6248.

[48] H. Liu, W. R. Cao, Y. Su, Y. Wang and X. H. Wang. Synthesis, characterization and photocatalytic performance of novel visible-light-induced Ag/BiOI. Applied Catalysis B: Environmental, 2012, 111-112, 271-279.

[49] X. A. Dong, W. D. Zhang, Y. J. Sun, J. Y. Li, W. L. Cen, Z. H. Cui, H. W. Huang and F. Dong. Visible-light-induced charge transfer pathway and photocatalysis mechanism on Bi semimetal@defective BiOBr hierarchical microspheres. Journal of Catalysis, 2018, 357, 41-50.

[50] F. Dong, T. Xiong, S. Yan, H. Q. Wang, Y. J. Sun, Y. X. Zhang, H. W. Huang and Z. B. Wu. Facets and defects cooperatively promote visible light plasmonic photocatalysis with Bi nanowires@BiOCl nanosheets. Journal of Catalysis, 2016, 344, 401-410.

[51] Q. Wang, W. Wang, L. L. Zhong, D. M. Liu, X. Z. Cao and F. Y. Cui. Oxygen vacancy-rich 2D/2D BiOCl-g-C_3N_4 ultrathin heterostructure nanosheets for enhanced visible-light-driven photocatalytic activity in environmental remediation. Applied Catalysis B: Environmental, 2018, 220, 290-302.

[52] Y. J. Wang, J. R. Jin, W. G. Chu, D. Cahen and T. He. Synergistic Effect of Charge Generation and Separation in Epitaxially Grown BiOCl/Bi_2S_3 Nano-Heterostructure. ACS Appl. Mater. Interfaces, 2018, 10, 15304-15313.

[53] J. Wang, G. K. Zhang, J. Li and K. Wang. Novel Three-Dimensional Flowerlike BiOBr/Bi_2SiO_5 p-n Heterostructured Nanocomposite for Degradation of Tetracycline: Enhanced Visible Light Photocatalytic Activity and Mechanism. ACS Sustainable Chem. Eng. 2018, 6, 14221-14229.

[54] P. Li, X. Zhao, C. J. Jia, H. G. Sun, L. M. Sun, X. F. Cheng, L. Liu and W. L. Fan. $ZnWO_4$/BiOI heterostructures with highly efficient visible light photocatalytic activity: the case of interface lattice and energy level match. J. Mater. Chem. A, 2013,1, 3421-3429.

[55] M. X. Ji, Y. L. Liu, J. Di, R. Chen, Z. G. Chen, J. X. Xia and H. M. Li. N-CQDs accelerating surface charge transfer of $Bi_4O_5I_2$ hollow nanotubes with broad spectrum photocatalytic activity. Applied Catalysis B: Environmental, 2018, 237, 1033-1043.

[56] Y. Bai, L. Q. Ye, T. Chen, L. Wang, X. Shi, X. Zhang and D. Chen. Facet-Dependent Photocatalytic N_2 Fixation of Bismuth-Rich Bi_5O_7I Nanosheets. ACS Appl. Mater. Interfaces, 2016, 8, 27661-27668.

[57] C. Y. Wang, X. Zhang, X. N. Song, W. K. Wang and H. Q. Yu. Novel $Bi_{12}O_{15}Cl_6$ Photocatalyst for the Degradation of Bisphenol A under Visible-Light Irradiation. ACS Appl. Mater. Interfaces, 2016, 8, 5320-5326.

[58] C. Y. Wang, X. Zhang, H. B. Qiu, W. K. Wang, G. X. Huang, J. Jiang, H. Q. Yu. Photocatalytic degradation of bisphenol A by oxygen-rich and highly visible-light responsive $Bi_{12}O_{17}Cl_2$ nanobelts. Applied Catalysis B: Environmental, 2017, 200, 659-665.

[59] D. J. Mao, J. L. Yuan, X. L. Qu, C. Sun, S. G. Yang and H. He. Size tunable Bi_3O_4Br hierarchical hollow spheres assembled with {0 0 1}-facets exposed nanosheets for robust photocatalysis against phenolic pollutants. Journal of Catalysis, 2019, 369, 209-221.

[60] Y. Bai, P. Yang, L. Wang, B. Yang, H. Q. Xie, Y. Zhou and L. Q. Ye. Ultrathin $Bi_4O_5Br_2$ nanosheets for selective photocatalytic CO_2 conversion into CO. Chemical Engineering Journal, 2019, 360, 473-482.

[61] X. Xiao, C. X. Zheng, M. L. Lu, L. Zhang, F. Liu, X. X. Zuo and J. M. Nan. Deficient $Bi_{24}O_{31}Br_{10}$ as a highly efficient photocatalyst for selective oxidation of benzyl alcohol into benzaldehyde under blue LED irradiation. Applied Catalysis B: Environmental, 2018, 228, 142-151.

[62] L. Q. Ye, Y. Deng, L. Wang, H. Q. Xie and F. Y. Su. Bismuth-Based Photocatalysts for Solar Photocatalytic Carbon Dioxide Conversion. ChemSusChem, 10.1002/cssc.201901196.

[63] J. Li, G. M. Zhan, Y. Yu and L. Z. Zhang. Superior visible light hydrogen evolution of Janus bilayer junctions via atomic-level charge flow steering. Nat. Commun., 2016, 7, 11480.

[64] X. Y. Xiao, J. Jiang and L. Z. Zhang. Selective oxidation of benzyl alcohol into benzaldehyde over semiconductors under visible light: The case of $Bi_{12}O_{17}Cl_2$ nanobelts. Applied Catalysis B: Environmental, 2013, 142-143, 487-493.

[65] J. Di, C. Zhu, M. X. Ji, M. L. Duan, R. Long, C. Yan, K. Z. Gu, J. Xiong, Y. B. She, J. X. Xia, H. M. Li and Z. Liu. Defect-Rich $Bi_{12}O_{17}Cl_2$ Nanotubes Self-Accelerating Charge Separation for Boosting Photocatalytic CO_2 Reduction. Angew. Chem. Int. Ed. 2018, 57, 14847-14851.

[66] Y. Z. Wang, X. Y. Huang, K. Q. Wang, L. L. Zhang, B. Wang, Z. B. Fang, Y. Zhao, F. Gao, P. Liu and W. H. Feng. Ag-modified ultrathin $Bi_{12}O_{17}Cl_2$ nanosheets: photo-assisted Ag exfoliation synthesis and enhanced photocatalytic performance. J. Mater. Chem. A, 2018, 6, 9200-9208.

[67] L. Shi, W. W. Si, F. X. Wang and W. Qi. Construction of 2D/2D layered g-C_3N_4/$Bi_{12}O_{17}Cl_2$ hybrid material with matched energy band structure and its improved photocatalytic performance. RSC Adv., 2018, 8, 24500-24508.

[68] C. Y. Zhou, C. Lai, P. Xu, G. M. Zeng, D. L. Huang, Z. H. Li, C. Zhang, M. Cheng, L. Hu, J. Wan, F. Chen, W. P. Xiong and R. Deng. Rational Design of Carbon-Doped Carbon Nitride/$Bi_{12}O_{17}Cl_2$ Composites: A Promising Candidate Photocatalyst for Boosting Visible-Light-Driven Photocatalytic Degradation of Tetracycline. ACS Sustainable Chem. Eng., 2018, 6, 6941-6949.

[69] G. P. He, C. L. Xing, X. Xiao, R. P. Hu, X. X. Zuo and J. M. Nan. Facile synthesis of flower-like $Bi_{12}O_{17}Cl_2$/Bi_2O_3 composites with enhanced visible light photocatalytic performance for

the degradation of 4-tert-butylphenol. Applied Catalysis B: Environmental, 2015, 170-171, 1-9.

[70] H. W. Huang, K. Xiao, Y. He, T. R. Zhang, F. Dong, X. Du and Y. H. Zhang. In situ assembly of BiOI@$Bi_{12}O_{17}Cl_2$ p-n junction: charge induceduniqueunique front-lateral surfaces coupling heterostructure with highexposure of BiOI {001} active facets for robust and nonselectivephotocatalysis. Applied Catalysis B: Environmental, 2016,199, 75-86.

[71] L. Hao, H. W. Huang, Y. X. Guo, X. Du, Y. H. Zhang. Bismuth oxychloride homogeneous phasejunction BiOCl/$Bi_{12}O_{17}Cl_2$ with unselectively efficient photocatalytic activity and mechanism insight. Applied Surface Science, 2017,420, 303-312.

[72] W. D. Zhang, X. A. Dong, B. Jia, J. B. Zhong, Y. J. Sun and F. Dong. 2D BiOCl/$Bi_{12}O_{17}Cl_2$ nanojunction: Enhanced visible light photocatalytic NO removal and in situ DRIFTS investigation. Applied Surface Science, 2018, 430, 571-577.

[73] S. Q. Jiang, L. Wang, W. C. Hao, W. X. Li, H. J. Xin, W. W. Wang and T. M. Wang. Visible-Light Photocatalytic Activity of S-Doped α-Bi_2O_3. J. Phys. Chem. C, 2015, 119, 14094-14101.

[74] J. Rong, T. Zhang, F. X. Qiu, X. S. Rong, X. L. Zhu and X. Y. Zhang. Preparation of hierarchical micro/nanostructured Bi_2S_3-WO_3 composites for enhanced photocatalytic performance. Journal of Alloys and Compounds, 2016, 685, 812-819.

[75] Y. F. Liu, W. Q. Yao, D. Liu, R. L. Zong, M. Zhang, X. G. Ma and Y. F. Zhu. Enhancement of visible light mineralization ability and photocatalytic activity of $BiPO_4$/BiOI. Applied Catalysis B: Environmental, 2015, 163, 547-553.

[76] J. J. Zheng, F. Chang, M. Z. Jiao, Q. Xu, B. Q. Deng and X. F. Hu. A visible-light-driven heterojuncted composite WO_3/$Bi_{12}O_{17}Cl_2$: Synthesis, characterization, and improved photocatalytic performance. Journal of Colloid and Interface Science, 2018, 510, 20-31.

[77] S. S. Gupta, M. Stadler, C. A. Noser, A. Ghosh, B. Steinhoff, D. Lenoir, C. P. Horwitz, K.-W. Schramm and T. J. Collins. Rapid Total Destruction of Chlorophenols by Activated Hydrogen Peroxide. Science, 2002, 296, 326-328.

[78] M. L. Wang, G. D. Fang, P. Liu, D. M. Zhou, C. Ma, D. J. Zhang and J. H. Zhan. Fe_3O_4@β-CD nanocomposite as heterogeneous Fenton-like catalystfor enhanced degradation of 4-chlorophenol (4-CP). Applied Catalysis B: Environmental, 2016, 188, 113-122.

[79] F. Chang, X. F. Wang, J. R. Luo, J. Wang, Y. C. Xie, B. Q. Deng and X. F. Hu. Ag/$Bi_{12}O_{17}Cl_2$ composite: A case study of visible-light-driven plasmonic photocatalyst. Journal of Molecular Catalysis A: Chemical, 2017, 427, 45-53.

[80] D. Wu, B. Wang, W. Wang, T. C. An, G. Y. Li, T. W. Ng, H. Y. Yip, C. M. Xiong, H. K. Lee and P. K. Wong. Visible-light-driven BiOBr nanosheets for highly facet-dependent photocatalytic inactivation of Escherichia coli. J. Mater. Chem. A, 2015, 3, 15148-15155.

[81] Y. G. Xu, Y. Ma, X. Y. Ji, S. Q. Huang, J. X. Xia, M. Xie, J. Yan, H. Xu and H. M. Li. Conjugated conducting polymers PANI decorated $Bi_{12}O_{17}Cl_2$ photocatalyst with extended light response range and enhanced photoactivity. Applied Surface Science, 2019, 464, 552-561.

[82] C. Y. Zhou, C. Lai, P. Xu, G. M. Zeng, D. L. Huang, C. Zhang, M. Cheng, L. Hu, J. Wan, Y. Liu, W. P. Xiong, Y. C. Deng and M. Wen. In Situ Grown AgI/$Bi_{12}O_{17}Cl_2$ Heterojunction Photocatalysts for Visible Light Degradation of Sulfamethazine: Efficiency, Pathway, and Mechanism. ACS Sustainable Chem. Eng. 2018, 6, 4174-4184.

[83] X. J. Wang, W. Y. Yang, F. T. Li, J. Zhao, R. H. Liu, S. J. Liu and B. Li. Construction of amorphous TiO_2/BiOBr heterojunctions via facets coupling for enhanced photocatalytic activity. Journal of Hazardous Materials, 2015, 292, 126-136.

[84] Z. K. Cui, H. T. Song, S. X. Ge, W. W. He and Y. W. Liu. Fabrication of BiOCl/BiOBr hybrid nanosheets with enhanced superoxide radical dominating visible light driven photocatalytic activity. Applied Surface Science, 2019, 467-468, 505-513.

[85] J. Fu, Y. L. Tian, B. B. Chang, F. N. Xi and X. P. Dong. BiOBr–carbon nitride heterojunctions: synthesis, enhanced activity and photocatalytic mechanism. J. Mater. Chem., 2012, 22, 21159-21166.

[86] F. Y. Wu, F. Chang, J. J. Zheng, M. Z. Jiao, B. Q. Deng, X. F. Hu and X. Q. Liu. Synthesis and Photocatalytic Performance of $Bi_{12}O_{17}Cl_2$ Semiconductors Calcined at Different Temperatures. Journal of Inorganic and Organometallic Polymers and Materials, 2018, 28, 721-730.

[87] A. Samadi-Maybodi and S. M. Pourali. Microwave-assisted aging synthesis of bismuth modified zeolite-P microspheres via BiOCl nanoflake transformation. Microporous and Mesoporous Materials, 2013, 167, 127-132.

[88] J. M. Song, C. J. Mao, H. L. Niu, Y. H. Shen and S. Y. Zhang. Hierarchical structured bismuth oxychlorides: self-assembly from nanoplates to nanoflowers via a solvothermal route and their photocatalytic properties. CrystEngComm, 2010, 12, 3875-3881.

[89] F. Chang, F. Y. Wu, W. J. Yan, M. Z. Jiao, J. J. Zheng, B. Q. Deng and X. F. Hu. Oxygen-rich bismuth oxychloride $Bi_{12}O_{17}Cl_2$ materials: construction, characterization, and sonocatalytic degradation performance. Ultrasonics-Sonochemistry, 2019, 50, 105-113.

[90] D. Wu, S. T. Yue, W. Wang, T. C. An, G. Y. Li, L. Q. Ye, H. Y. Yip and P. K. Wong. Influence of photoinduced Bi-related self-doping on the photocatalytic activity of BiOBr nanosheets. Applied Surface Science, 2017, 391, 516-524.

[91] D. Wu, S. T. Yue , W. Wang, T. C. An, G. Y. Li, H. Y. Yip, H. J. Zhao and P. K. Wong. Boron doped BiOBr nanosheets with enhanced photocatalytic inactivation of Escherichia coli. Applied Catalysis B: Environmental, 2016, 192, 35-45.

[92] H. Wang, D. Y. Yong, S. C. Chen, S. L. Jiang, X. D. Zhang, W. Shao, Q. Zhang, W. S. Yan, B. C. Pan and Y. Xie. Oxygen-Vacancy-Mediated Exciton Dissociation in BiOBr for Boosting Charge-Carrier-Involved Molecular Oxygen Activation. J. Am. Chem. Soc. 2018, 140, 1760-1766.

[93] W. Chen, T. Y. Liu, T. Huang, X. H. Liu and X. J. Yang. Novel mesoporous P-doped graphitic carbon nitride nanosheets coupled with $ZnIn_2S_4$ nanosheets as efficient visible light driven heterostructures with remarkably enhanced photo-reduction activity. Nanoscale, 2016, 8, 3711-3719.

[94] W. D. Zhang, X. A. Dong, Y. Liang, Y. J. Sun and F. Dong. Ag/AgCl nanoparticles assembled on $BiOCl/Bi_{12}O_{17}Cl_2$ nanosheets: Enhanced plasmonic visible light photocatalysis and in situ DRIFTS investigation. Applied Surface Science, 2018, 455, 236-243.

[95] J. Xu, L. W. Zhang, R. Shi and Y. F. Zhu. Chemical exfoliation of graphitic carbon nitride for efficient heterogeneous photocatalysis. J. Mater. Chem. A, 2013,1, 14766-14772.

[96] Y. Q. Jia, Y. X. Yang, Y. N. Guo, W. Guo, Q. Qin, X. Yang and Y. H. Guo. Simulated sunlight photocatalytic degradation of aqueous p-nitrophenol and bisphenol A in a Pt/BiOBr film-coated quartz fiber photoreactor. Dalton Trans., 2015, 44, 9439-9449.

[97] L. W. Yang, L. L. Liang, L. J. Wang, J. C. Zhu, S. W. Gao and X. F. Xia. Accelerated photocatalytic oxidation of carbamazepine by a novel 3D hierarchical protonated g-C_3N_4/BiOBr heterojunction: Performance and mechanism. Applied Surface Science, 2019, 473, 527-539.

[98] L. Shi, J. Y. Ma, L. Z. Yao, L. S. Cui and W. Qi. Enhanced photocatalytic activity of $Bi_{12}O_{17}Cl_2$ nano-sheets via surface modification of carbon nanotubes as electron carriers. Journal of Colloid and Interface Science, 2018, 519, 1-10.

[99] G. P. He, C. L. Xing, X. Xiao, R. P. Hu, X. X. Zuo and J. M. Nan. Facile synthesis of flower-like $Bi_{12}O_{17}Cl_2/Bi_2O_3$ composites with enhanced visible light photocatalytic performance for the degradation of 4-tert-butylphenol. Applied Catalysis B: Environmental, 2015, 170-171, 1-9.

[100] A. A. Dubale, I. N. Ahmed, X. H. Chen, C. Ding, G. H. Hou, R. F. Guan, X. M. Meng, X. L. Yang and M. H. Xie. A highly stable metal–organic framework derived phosphorus doped carbon/Cu_2O structure for efficient photocatalytic phenol degradation and hydrogen production. J. Mater. Chem. A, 2019, 7, 6062-6079.

[101] H. W. Huang, Y. He, Z. S. Lin, L. Kang and Y. H. Zhang. Two Novel Bi-Based Borate Photocatalysts: Crystal Structure, Electronic Structure, Photoelectrochemical Properties, and Photocatalytic Activity under Simulated Solar Light Irradiation. J. Phys. Chem. C, 2013, 117, 22986-22994.

[102] L. Wang, J. Ding, Y. Y. Chai , Q. Q. Liu , J. Ren , X. Liu and W. L. Dai. CeO_2 nanorod/g-C_3N_4/N-rGO composite: enhanced visible-light-driven photocatalytic performance and the role of N-rGO as electronic transfer media. Dalton Trans., 2015, 44,11223-11234.

[103] F. Xie, Y. Zhang, X. He, H. D. Li, X. Y. Qiu, W. C. Zhou, S. T. Huo and Z. Y. Tang. First achieving highly selective oxidation of aliphatic alcohols to aldehydes over photocatalysts. J. Mater. Chem. A, 2018, 6, 13236-13243.

[104] X. M. Zhang, G. B. Ji, Y. S. Liu, X. G. Zhou, Y. Zhu, D. N. Shi, P. Zhang, X. Z. Cao and B. Y. Wang. The role of Sn in enhancing the visible-light photocatalytic activity of hollow hierarchical microspheres of the Bi/BiOBr heterojunction. Phys. Chem. Chem. Phys., 2015, 17, 8078-8086.

[105] X. M. Jia, J. Cao, H. L. Lin, M. Y. Zhang, X. M. Guo and S. F. Chen. Transforming type-I to type-II heterostructure photocatalyst viaenergy band engineering: A case study of I-BiOCl/I-BiOBr. Applied Catalysis B: Environmental, 2017, 204, 505-514.

[106] J. Ding, Z. Dai, F. Qin, H. P. Zhao, S. Zhao and R. Chen. Z-scheme $BiO_{1-x}Br$ /$Bi_2O_2CO_3$ photocatalyst with rich oxygen vacancy as electron mediator for highly efficient degradation of antibiotics. Applied Catalysis B: Environmental, 2017, 205, 281-291.

[107] S. J. He, Q. F. Rong, H. Y. Niu and Y. Q. Cai. Construction of a superior visible-light-driven photocatalyst based on a C_3N_4 active centre-photoelectron shift platform-electron withdrawing unit triadic structure covalent organic framework. Chem. Commun., 2017, 53, 9636-9639.

[108] Y. K. Huang, S. F. Kang, Y. Yang, H. F. Qin, Z. J. Ni, S. J. Yang and X. Li. Facile synthesis of Bi/Bi_2WO_6 nanocomposite with enhanced photocatalytic activity under visible light. Applied Catalysis B: Environmental, 2016, 196, 89-99.